Proton and neutron density distributions for $A = 16$–58 nuclei

B A Brown, S E Massen† and P E Hodgson

Nuclear Physics Laboratory, Department of Nuclear Physics, University of Oxford, Keble Road, Oxford OX1 3RD, UK

Abstract. A new method of calculating nuclear charge and matter distributions is described. It uses the sum of the squares of single-particle wavefunctions to give a first approximation and then iterates the proton and neutron densities in a formalism that takes into account the interaction between these densities and between the valence and core nucleons. The single-particle potentials are adjusted to give the experimental centroid separation energies, and configuration mixing is included using shell-model occupation probabilities. The method is applied to the core nuclei ^{16}O and ^{40}Ca, to their isotopes and to other nuclei in the sd and pf shells. Detailed comparisons are made with all available experimental data on nuclear charge and matter distributions.

1. Introduction

This work was inspired by the great improvement in the quality and quantity of the experimental determinations of charge and matter distributions in light nuclei in the last few years. For example, the energies of muonic atom x-ray transitions have been used to determine the mean square radii with extremely high accuracy for stable isotopes above $A = 40$ (Wohlfahrt *et al* 1978 and private communication, Shera *et al* 1976). Data from atomic spectra are beginning to complement the muonic atom experiments, especially for the isotopes with very small abundances (Brandt *et al* 1978) as well as unstable isotopes (Huber *et al* 1978). Electron scattering experiments have been extended up to a high enough momentum transfer ($q \simeq 4 \, \text{fm}^{-1}$) for them to be sensitive for the first time to the high-frequency density oscillations ($\lambda \simeq 2 \, \text{fm}$) which are expected in the nuclear shell model (Sick 1974a,b, Sick *et al* 1975, Li *et al* 1974, Miska *et al* 1979). Careful analysis of hadron scattering is beginning to give information on the neutron distributions (Alkhazov *et al* 1976, 1977, Chaumeaux *et al* 1977, Friedman *et al* 1978, Varma and Zamick 1977). Information on 'individual orbit' sizes is being obtained from one-nucleon-transfer experiments (Durell *et al* 1977, Friedman *et al* 1977) and magnetic electron scattering (deWitt Huberts *et al* 1977). The theoretical and experimental situation up to early 1975 has been reviewed by Barrett and Jackson (1977). The recent work on electron scattering has been reviewed at a meeting in Amsterdam (Frois 1978, deWitt Huberts 1978) and extensive summaries of the analysis of high-energy proton scattering have recently been made (Alkhazov *et al* 1978, Chaumeaux *et al* 1978).

† Present address: Department of Theoretical Physics, University of Thessaloniki, Thessaloniki, Greece.

In the present work we wish to investigate what can be learned by applying a new method of analysis to the results of some of these experiments. Previously, the Hartree–Fock method has provided the most reliable and least arbitrary tool for nuclear density calculations. In an harmonic oscillator shell-model basis the Hartree–Fock method takes into account the smearing of the orbit occupation probabilities far from the Fermi surface. In this work we want to emphasise the important problems associated with the diffuseness of the orbit occupation probabilities *near* the Fermi surface as revealed by large-basis shell-model calculations. Thus we need to develop a simple approach which can combine aspects of the Hartree–Fock method with the complex configuration mixing encountered in the shell-model calculations.

Provided that the wavefunction can be written as a single Slater determinant, for example as a state which is a function of the intrinsic deformation, the Hartree–Fock method can be used to obtain the single-particle wavefunctions and the average density. The quantitative success of Hartree–Fock calculations is, however, limited by the lack of knowledge of the exact nucleon–nucleon interaction and its renormalisation in finite nuclei. Hence one must resort to phenomenological interactions whose parameters are chosen to reproduce some observed properties such as centroid binding energies and RMS radii. These parameters can then be used to construct equivalent local potentials (Dover and Van Giai 1972) that can be compared with the single-particle potentials such as the Woods–Saxon potential which have often been used for the analysis of experiments. At this point it is clear that if the Hartree–Fock calculation is not in agreement with some aspect of the phenomenological single-particle model it may be due to an undetermined parameter or an approximation in the two-body interaction. Hence, for any particular nucleus a phenomenological nucleon–*nucleus* interaction remains a viable alternative for quantitative calculations. However, what is seriously lacking in the Woods–Saxon model is a method of describing the microscopic variation in the parameters from nucleus to nucleus other than by some *ad hoc* adjustment. In the Hartree–Fock approach a microscopic variation is built in due to the self-consistency between the potential and the density. In the present calculations we take an intermediate approach and use a local self-consistent potential which is based on the parameters of the optical model. This method will be outlined below and discussed in detail in § 2.

The major source of concern in the application of the Hartree–Fock method to light nuclei is that the mean-field approximation is not good because even the spherical nuclei (^{16}O, ^{40}Ca) do not have good closed shells (compared with ^{208}Pb). One of the main goals of the present work is to study the effect of complex configurations on the neutron and proton densities. This is done by first taking occupation probabilities from large-basis shell-model calculations and then making any adjustments which are necessary to obtain agreement with the experimental densities. As will be shown in § 3, these results can be compared with the analysis of other experiments (such as the one-nucleon-transfer spectroscopic factors) which are also sensitive to the occupation probabilities.

In outline, our method is as follows. In the first step we carry out a standard Woods–Saxon calculation for a 'closed shell' nucleus, for example ^{16}O, in which the parameters for protons are fixed to reproduce the experimental proton centroid energies and RMS charge radius. This determines the parameters V_0 and R in the expression (the spin–orbit term will not be included for the illustration)

$$V_p(r) = V_0 f(r) + V_C(r)$$
$$f(r) = (1 + \exp[(r - R)/a])^{-1}$$

(1)

where $V_C(r)$ is the Coulomb potential. Then in order to calculate the neutron distribution, the term proportional to $(N - Z)/A$ in the nucleon–nucleus potential is replaced by $\rho_1(r)/\rho_0(r)$ where

$$\rho_1(r) = \rho_n(r) - \rho_p(r)$$
$$\rho_0(r) = \rho_n(r) + \rho_p(r) \tag{2}$$

where $\rho(r)$ is the radial density, and the self-consistent solution to the coupled equations for neutrons and protons with

$$V_p(r) = \left(V_0 + V_1 \frac{\rho_1(r)}{\rho_0(r)}\right)f(r) + V_C(r)$$
$$V_n(r) = \left(V_0 - V_1 \frac{\rho_1(r)}{\rho_0(r)}\right)f(r) \tag{3}$$

is found by straightforward iteration.

To calculate the densities of other nuclei, for example ^{17}O, ^{18}O, $^{20}Ne, \ldots$, equation (3) is written in the form

$$V_p(r) = (V_0\rho_0(r) + V_1\rho_1(r))F(r) + V_C(r)$$
$$V_n(r) = (V_0\rho_0(r) - V_1\rho_1(r))F(r) \tag{4}$$

where

$$F(r) = f(r)/\rho_0^c(r)$$

and $\rho_0^c(r)$ denotes the density of the 'closed shell' (core) particles. Again the neutron and proton densities are found from an iteration of the coupled equations. As will be discussed in detail in § 2.4, equation (4) contains the important effect of polarisation of the core by the valence particles.

With the above formalism it is particularly appropriate to investigate changes in the neutron and proton distributions relative to the core nuclei ^{16}O and ^{40}Ca; in fact, in many experiments this is what is determined most accurately. There are essentially *no free parameters* in the potential for the density differences because they are all fixed by the core nuclei. It is now very easy to calculate the effect of configuration mixing on the density differences. For example, we can see if reasonable configuration mixing is able to account for the detailed structure of the charge density change as well as the root-mean-square radii. It is clear that this method is sensitive mainly to the changes in the configurations relative to the core nuclei.

With the present model we want to calculate all the important aspects of the neutron and proton densities which are determined by the experiments outlined at the beginning of this section. Most of the data concern the charge distribution. The relations between the charge and the proton distributions are given in § 2.5, and the conclusions based on the comparison with experiment are discussed in § 3. The neutron densities and the RMS radii of individual orbits are discussed in §§ 4 and 5 respectively. We have also calculated the Coulomb energies, but since these are only indirectly related to the displacement energies (the difference in binding energies) of mirror nuclei they will be discussed in a separate paper (Brown *et al* 1979, unpublished). The conclusions are summarised in § 6.

2. Details of the method

2.1. Basic formulae and notation

Even though the basic formulae we use are standard, it is worth summarising them here so that it is clear exactly how we use them and to set the notation for the following sections.

The standard Woods–Saxon potential is given by

$$V(r) = \left(V_0 - 2t_z V_1 \frac{(N - Z)}{A} \right) f(r) + V_{ls}(r) \tag{5}$$

where

$$f(r) = (1 + \exp[(r - R)/a])^{-1}$$

$$V_{ls}(r) = V_{ls} \frac{1}{r} \frac{\mathrm{d} f_{ls}(r)}{\mathrm{d} r} \boldsymbol{l} \cdot \boldsymbol{\sigma} \tag{6}$$

$$f_{ls}(r) = (1 + \exp[(r - R_{ls})/a_{ls}])^{-1}$$

and $t_z = \frac{1}{2}$ for neutrons and $t_z = -\frac{1}{2}$ for protons.

The solutions to the Schrödinger equation are given by

$$\psi_{nljm}(r, \theta, \phi) = \frac{1}{r} U_{nlj}(r) \chi_{ljm}(\theta, \phi) \tag{7}$$

where $U(r)$ is a solution of the radial equation

$$\frac{\hbar^2}{2m} U''(r) + \left(\varepsilon_{nlj} - V(r) - \frac{\hbar^2}{2m} \frac{l(l + 1)}{r^2} \right) U(r) = 0. \tag{8}$$

For protons $V(r)$ includes the Coulomb potential.

In the many-particle system the total density is easily found for a closed-shell configuration, as the angular integral can be carried out giving the following spherical density:

$$\rho(r) = \sum_{\substack{\text{occupied} \\ nlj}} \frac{(2j + 1)}{4\pi} \left| \frac{U_{nlj}(r)}{r} \right|^2. \tag{9}$$

In the general case, even when there are not closed shells, we will make the following approximation for the average total density:

$$\rho_n(r) = \sum_{nlj} \frac{n_n(nlj)}{4\pi} \left| \frac{U_{nljn}(r)}{r} \right|^2$$

$$\rho_p(r) = \sum_{nlj} \frac{n_p(nlj)}{4\pi} \left| \frac{U_{nljp}(r)}{r} \right|^2 \tag{10}$$

where $n_n(nlj)$ and $n_p(nlj)$ are the neutron and proton occupation probabilities for the orbit nlj. These formulae are exact, however, for the $J = 0$ ground states of even–even nuclei. The densities are normalised so that

$$\int \rho_n(r) \, \mathrm{d}\tau = N \qquad \int \rho_p(r) \, \mathrm{d}\tau = Z. \tag{11}$$

The RMS radii will be denoted by r_n and r_p where, for example,

$$r_n^2 = \frac{\int \rho_n(r) r^4 dr}{\int \rho_n(r) r^2 dr}. \tag{12}$$

Since the method of calculation involves an iteration in which the density and potential are related, it is easy to use a Coulomb potential calculated from the proton distribution

$$V_C(r) = e \int \frac{\rho_p(r')}{|\vec{r} - \vec{r}'|} d\tau'$$

$$= 4\pi e \left(\frac{1}{r} \int_0^r \rho_p(r') r'^2 \, dr' + \int_r^\infty \rho_p(r') r' \, dr' \right). \tag{13}$$

The Coulomb exchange term resulting from the antisymmetrisation of the many-body wavefunction is small and will be neglected (although, of course, it cannot be neglected for an accurate calculation of Coulomb energy differences between analogue states).

2.2. The model for closed-shell nuclei

Consider the standard method of calculating neutron and proton densities using the Woods–Saxon potential in an $N = Z$ nucleus. In equation (5) there will be three important parameters, V_0, R and a, and these can be adjusted to reproduce single-particle energies of orbits near the Fermi surface and the RMS charge radius. These parameters are found to give too small binding energies for the deeply-bound orbits and the reasons for this can be understood from Hartree–Fock calculations as resulting from the non-local and velocity-dependent aspects of the nuclear interaction. Approximations have been developed to incorporate nonlocality into the Woods–Saxon calculations (Perey 1963), but it is adequate and more straightforward for the present investigation to take this into account by keeping a local potential and adjusting V_0 to reproduce the centroid energy for each orbit. We do this by adjusting V_{ls} for each spin–orbit pair separation and V_0 for each spin–orbit pair centroid. We take standard values for R_{ls}, a_{ls} and a, namely $1 \cdot 1 A^{1/3}$ fm, $0 \cdot 65$ fm and $0 \cdot 65$ fm respectively. Having a different potential for each orbit introduces non-orthogonality corrections into the calculation of the spherical densities (Malaguti *et al* 1978) but we have not included this correction since subsidiary calculations showed that it has very little effect on the results presented here.

If this procedure is carried out for the single-particle energies of both neutrons and protons in an $N = Z$ nucleus then it is usually found that V_0 is not the same for the protons and neutrons in a given orbital. This is a way of stating the well known Nolen–Schiffer anomaly (Nolen and Schiffer 1969), and indeed it may be that the nuclear force is actually charge asymmetric. However, in this work one of our interests is in calculating the proton and neutron density difference to see whether or not the data are consistent with a charge-symmetric interaction. To this end, it is easy to see that for $N = Z$ equation (5) will *not* give a self-consistent solution for the difference between the proton and neutron densities because the asymmetry potential which is proportional to V_1 vanishes. If V_0 is the same for protons and neutrons then, for example, in ^{40}Ca we find equation (5) gives $r_n - r_p = -0 \cdot 092$ fm. This difference is due to the Coulomb potential for protons.

We incorporate self-consistency by replacing $(N - Z)/A$ by $\rho_1(r)/\rho_0(r)$, where $\rho_1(r) = \rho_n(r) - \rho_p(r)$ and $\rho_0(r) = \rho_n(r) + \rho_p(r)$. Thus equation (5) becomes

$$V(r) = \left(V_0 - 2t_z V_1 \frac{\rho_1(r)}{\rho_0(r)} \right) f(r) + V_{ls}(r). \tag{14}$$

Now if the potential of equation (14) is used to solve self-consistently for the proton and neutron wavefunctions the difference in $r_n - r_p$ is reduced almost by a factor of two to a value of -0.056 fm. This result depends, of course, on V_1 and we have used a value of $V_1 = -30$ MeV which is an average of the values found from an analysis of the single-particle binding-energy systematics of $N \neq Z$ nuclei in the region $A = 35$–65 (Millener and Hodgson 1973). In the calculation V_0 and V_{ls} for each orbit are fixed from the proton binding energies since they are more accurately known than the neutron binding energies.

The difference $r_n - r_p = -0.056$ fm obtained using equation (14) is similar to the results of spherical Hartree–Fock calculations for ^{40}Ca. For example, from Beiner *et al* (1975), who used various Skyrme (S) forces, $r_n - r_p = -0.044$(SIII), -0.046(SIV) and -0.047(SV). Most Hartree–Fock calculations give values very similar to those obtained by Beiner *et al* (see table 2.1 of Barrett and Jackson 1978); however the value of $r_n - r_p = -0.034$ fm obtained by Lee and Cusson (1972) is exceptionally small. In the hydrodynamical model (Myers 1978) an even smaller value of $r_n - r_p = -0.02$ fm is obtained.

In figure 1 the density difference $\rho_p(r) - \rho_n(r)$ for ^{40}Ca is plotted for $V_1 = 0$ (in which case equations (5) and (14) are equivalent) and $V_1 = -30$ MeV. (The notation ^{40}Ca(IIB) in figure 1 will be explained below.) It is seen that the self-consistent density difference is about half of the value obtained with $V_1 = 0$ at every point. Also shown is the symmetry potential term of equation (14)

$$V_{sym}(r) = V_1 \frac{\rho_1(r)}{\rho_0(r)} f(r). \tag{15}$$
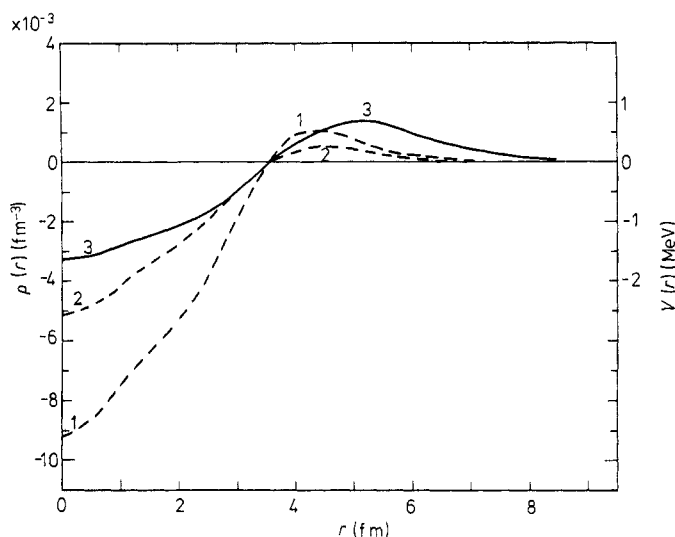

Figure 1. Isovector density and potential in ^{40}Ca using the occupation number set IIB discussed in § 3.5. The results with a closed-shell configuration (IIA) are essentially the same as those presented here obtained with a non-closed-shell configuration (IIB). 1, the isovector density obtained with a standard Woods–Saxon potential (equation (5); $\rho_p(r)$–$\rho_n(r)$, $V_1 = 0$); 2, the isovector density obtained by a self-consistent solution using the potential of equation (14) as discussed in § 2.2 ($\rho_p(r)$–$\rho_n(r)$, $V_1 = -30$ MeV); 3, the symmetry potential given by equation (15) ($V_1 = -30$ MeV).

2.3. Extension of the model to non-closed-shell nuclei

Consider first the standard methods of using equation (5) for some nucleus between ^{16}O and ^{40}Ca. The radius R is often parametrised in the form $R = r_0 A^{1/3} + b$. This form is chosen because it is well known that the nuclear density saturates and hence the nuclear radius goes as $A^{1/3}$. However, this is a global property that depends on an averaging of shell effects and hence there is no *a priori* justification for using this parametrisation for quantitative calculations over a small mass region, especially for light nuclei. Thus one may try to introduce another parameter such as $R = r_0 A^{\lambda/3} + b$ or even try to find a best value of R for every nucleus, but what one learns in such cases is often 'lost' in the parameters.

To avoid this arbitrariness we make a simple extension of equations (5) and (14) using the idea of self-consistency. To this end equation (14) for the closed-shell nuclei is rewritten in the form

$$V(r) = (V_0 \rho_0(r) - 2t_z V_1 \rho_1(r))F(r) + V_{ls}(r) \tag{16}$$

where $F(r) = f(r)/\rho_0(r)$. The form of this equation is interpreted in the following way: the average potential depends linearly on the density, as one obtains with a delta function two-body interaction, and the function $F(r)$ takes into account the finite-range and velocity-dependent aspects of the nuclear force. The function $F(r)$ prevents the nucleus from collapsing when a self-consistent calculation is carried out.

Then for the calculation of other nuclei $F(r)$ is taken as a *fixed* quantity given by

$$F^c(r) = f(r)/\rho_0^c(r) \tag{17}$$

where the label c refers to the core density which is obtained using the occupation probabilities of the 'closed-shell' nuclei ^{16}O or ^{40}Ca. For flexibility the potential parameters V_0 and V_1 are divided into core and valence parameters V^c and V^v and we have finally

$$V(r) = \left[V_0^c \rho_0^c(r) + V_0^v \rho_0^v(r) - 2t_z(V_1^c \rho_1^c(r) + V_1^v \rho_1^v(r)) \right] F^c(r) + V_{ls}(r). \tag{18}$$

For the results of the calculations presented here we have used folded densities $\tilde{\rho}(r)$ in place of $\rho(r)$ in the above equations which relate the density and the potential. The densities $\tilde{\rho}(r)$ were obtained by folding the point neutron and proton distributions with a gaussian, $\exp(-r^2/\mu^2)$, with $\mu = 0.65$ fm. This is a rather arbitrary procedure which may simulate the finite range of the interaction between the core and valence particles.

In this equation the occupation probabilities which determine the core density $\rho^c(r)$ are fixed quantities whereas the occupation probabilities which determine the valence density $\rho^v(r)$ are given by $n^v(nlj) = n(nlj) - n^c(nlj)$ and vary from nucleus to nucleus. Notice that in general $n^v(nlj)$ may be positive or negative non-integers (for example see § 3.7 and table 11), but that the total number of valence particles $\Sigma n^v(nlj) = n^v$ must be an integer.

All of the parameters in equation (18) are determined from the calculations for ^{16}O and ^{40}Ca as described in § 2.2 except for the two constants V_0^v and V_1^v. Once V_0^v and V_1^v are chosen all parameters are determined and the densities are calculated by a self-consistent solution using equation (18) for the nuclear potential. A few of the calculations presented here, namely those for the nuclei plus or minus one nucleon removed from ^{40}Ca, have been carried out using $V_0^v = -50$ MeV and $V_1^v = -30$ MeV which represent typical average values for these parameters. However, for most calculations we considered it more appropriate to adjust V_0^v and V_1^v in order to reproduce the correct change in centroid energy of the lowest valence orbit outside the core when a 'filled shell' of neutrons is added. For example, the experimental $d_{5/2}$ neutron single-particle energy
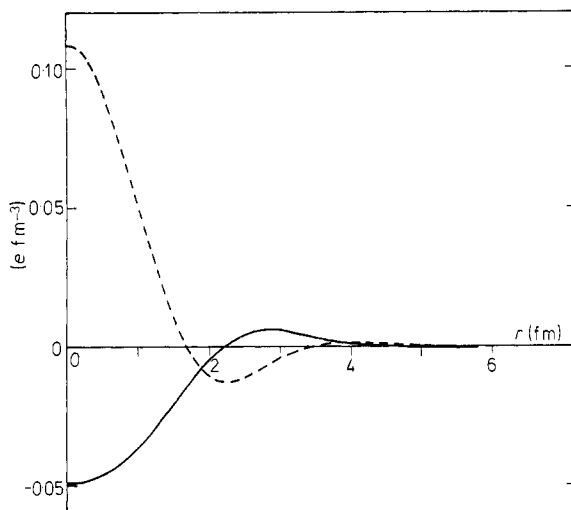
Figure 2. The theoretical charge density difference $4\pi\Delta\rho(r)_{ch}$ between ^{17}O and ^{16}O as discussed in § 2.4. The two curves correspond to the valence neutron in a $1d_{5/2}$ (full curve) and a $2s_{1/2}$ (broken curve) state. The comparison of the $1d_{5/2}$ curve with experiment is given in figure 4 and discussed in § 3.1.

changes from -4.14 MeV in ^{16}O to -6.71 MeV in ^{22}O while the $d_{5/2}$ proton single-particle energy changes from -0.60 MeV in ^{16}O to -13.42 MeV in ^{22}O (i.e. BE(^{23}F) $-$ BE(^{22}O) $= 13.42$ MeV). To reproduce this change in our calculation we need to choose a valence interaction with $V_0^v = -41$ MeV and $V_1^v = -28$ MeV. Similarly, in order to reproduce the change in the $f_{7/2}$ neutron and proton single-particle energies between ^{40}Ca and ^{48}Ca we need $V_0^v = -32$ MeV and $V_1^v = -21$ MeV.

2.4. The effect of core polarisation

It is interesting and instructive to consider the self-consistent densities obtained using equation (18) in the relatively simple case of ^{17}O, which we will assume, for this example, can be represented by a valence neutron outside ^{16}O. In particular, we are interested in the change in the proton distribution between ^{16}O and ^{17}O since the change in the charge distribution can be determined accurately by electron scattering experiments.

The change in the proton potential between ^{16}O and ^{17}O given by equation (18) is approximately

$$\Delta V_p(r) \simeq (V_0^v + V_1^v)\rho_n^v(r)F^c(r) \tag{19}$$

where $\rho_n^v(r)$ is the density of the valence neutron. Thus all the protons feel a relatively large change in the potential which is proportional to the density of the valence neutron; it is large because $V_0^v + V_1^v$ is large.

The change in the charge density obtained when the valence neutron is in the $2s_{1/2}$ or $1d_{5/2}$ orbits is shown in figure 2 (the exact relation between the charge and proton density will be discussed below, but for this example they are essentially identical). The density changes are large and very dependent on the valence configuration. For the $d_{5/2}$ neutron, which has a maximum in the density at $r \simeq 2.4$ fm, the core protons are pulled out resulting in a decrease in the centre, whereas for the $s_{1/2}$ neutron, which has a maximum density at $r = 0$, the opposite is true. However, the changes in the RMS

radii are small, $r_p(^{17}O) - r_p(^{16}O) = 0.006$ fm with a $d_{5/2}$ neutron and 0.003 fm with a $s_{1/2}$ neutron.

These results will be compared with experiment in § 3.2. Since the change given by equation (19) is linear in the number of valence neutrons the change in the charge distribution is very dramatic when there are many valence neutrons, and the interesting case of ^{48}Ca will be discussed in detail below in § 3.5.

It should be pointed out that this effect is not new to our calculation. It is obtained with equation (5), although in a way that ignores shell effects such as the difference between the $d_{5/2}$ and $s_{1/2}$ cases discussed above. It is, of course, also built into Hartree–Fock calculations (Sprung *et al* 1976). However, a unique feature of the present calculation is that $\rho^v(r)$, on which the core polarisation effect depends, is determined by shell-model calculations rather than by assuming a single Slater determinant.

2.5. Calculation of the charge distribution

Measurements of the charge distribution in nuclei with leptonic probes have reached a level of precision where it is necessary to consider the differences between the proton and the charge distributions. For these calculations we follow Bertozzi *et al* (1972), Friar and Negele (1975) and Chandra and Sauer (1976). The total charge distribution is written as a sum of three terms, $\rho(r)_{ch}^p$ which comes from the finite charge distribution of the proton folded with the point proton distribution, $\rho(r)_{ch}^n$ which comes from the finite charge distribution of the neutron folded with the point neutron distribution, and $\rho(r)_{ch}^{ls}$ which is a relativistic correction which depends on $l \cdot \sigma$. Thus we have

$$\rho(r)_{ch} = \rho(r)_{ch}^p + \rho(r)_{ch}^n + \rho(r)_{ch}^{ls}. \tag{20}$$

The experimental charge form factors for the proton and neutron can be parametrised (not uniquely) as a sum of gaussians for the density distributions:

$$G(r) = \sum \theta_i \exp(-r^2/r_i^2)/(\pi r_i^2)^{3/2}. \tag{21}$$

Two gaussians are needed for the neutron ($\Sigma\theta_i = 0$) and three gaussians for the proton ($\Sigma\theta_i = 1$). The parameters θ_i and r_i from Chandra and Sauer are given in table 1. The proton RMS radius of 0.88 fm from this sum of three gaussians is a little larger than the standard value of 0.83 fm needed if a dipole form factor is used; however, as pointed out by Chandra and Sauer, the proton charge form factor for high q is not well fitted by the dipole form.

Table 1. Parameters of the nucleon charge distributions[a].

	Proton	Neutron
θ_1	0.506	1
θ_2	0.328	-1
θ_3	0.166	0
r_1^2 (fm^2)	0.432	0.469
r_2^2 (fm^2)	0.139	0.546
r_3^2 (fm^2)	1.526	—
Mean square radius (fm^2)	0.775	-0.116

[a] Chandra and Sauer (1976).

The correction due to spurious centre-of-mass motion and the Darwin–Foldy relativistic correction are included in equation (21) by replacing r_i^2 by

$$r_i^2 + \tfrac{1}{2}(\hbar/mc)^2 - (b^2/A) \tag{22}$$

where $b^2 = 41\cdot465/\hbar\omega \simeq A^{1/3}$ fm^2 and $\hbar/mc = 0\cdot21$ fm.

The proton charge distribution is given by

$$\rho(r)_{ch}^p = \int \rho_p(r')G(|\boldsymbol{r} - \boldsymbol{r}'|)d\tau'$$

$$= \frac{1}{\sqrt{\pi}} \sum_i \frac{\theta_i}{r_i} \int_0^\infty \frac{r'}{r} \rho_p(r')\left(\exp\left[-\left(\frac{r - r'}{r_i}\right)^2\right] - \exp\left[-\left(\frac{r + r'}{r_i}\right)^2\right]\right)dr' \tag{23}$$

and similarly for $\rho(r)_{ch}^n$. This formula is equivalent to the operation $F^{-1}\{F[\rho(r)]F[G(r)]\}$ where F is the Fourier transform.

The relativistic spin–orbit correction using the factorisation approximation introduced by Bertozzi *et al* (1972) is given by

$$\rho(r)_{ch}^{ls} = -\left(\frac{\hbar}{mc}\right)^2 \left(\sum_{nlj} \tfrac{1}{2}n_p(nlj)l'\mu'_p \frac{1}{r^2}\frac{d}{dr}(r\rho_p^{nlj}(r)) + \sum_{nlj} \tfrac{1}{2}n_n(nlj)\,l'\mu_n \frac{1}{r^2}\frac{d}{dr}(r\rho_n^{nlj}(r))\right) \tag{24}$$

where $\rho^{nlj}(r)$ is the density of each orbit. $l' = l$ for $j = l + \tfrac{1}{2}$, $l' = -(l + 1)$ for $j = l - \tfrac{1}{2}$, $\mu'_p = \mu_p - \tfrac{1}{2} = 2\cdot29$ and $\mu_n = -1\cdot91$. This correction is only important for the orbits which have $n_p(nlj) \neq n_n(nlj)$ and thus has only been calculated for the valence densities. The normalisation of $\rho(r)_{ch}$ is

$$\int \rho(r)_{ch}\, d\tau = Ze. \tag{25}$$

The energy shifts of the muonic x-rays have been analysed in terms of the model-independent Barrett radii defined by

$$\langle r^k e^{-\alpha r}\rangle = \frac{4\pi}{Z} \int \rho_{ch}(r)r^{k+2}e^{-\alpha r}\, dr \tag{26}$$

where k and α are constants (Barrett 1970). For light nuclei, since the muonic wavefunction is nearly constant over the nuclear volume, $k \simeq 2$ and $1/\alpha$ is large compared with the nuclear radius, so that the model dependence in the RMS radii determined from these experiments for light nuclei is small.

Since it is interesting to compare the RMS radii obtained in muonic atom experiments with those determined by electron scattering, the following formula has been used to convert Barrett radii into 'model-independent' RMS radii:

$$(r_{ch})_\mu^W = (\langle r^k e^{-\alpha r}\rangle_{\mu-exp})^\gamma \left(\frac{(r_{ch})_{th}^W}{(\langle r^k e^{-\alpha r}\rangle_{th}^W)^\gamma}\right) \tag{27}$$

where γ is an arbitrary constant of the order of $1/k$ chosen so that the term in large round brackets is near unity; we have used $\gamma = 0\cdot52$. The defining labels of the theoretical model are denoted by W. Thus, in an approximation, $(r_{ch})_\mu^W$ is the RMS radius that would be obtained if the muonic x-ray shifts were analysed using the theoretical charge density shape (presumably 'correct') instead of the shape which was actually used in the analysis (i.e., the Fermi shape which is presumably not as 'correct').

3. Charge densities

3.1. The nucleus ^{16}O

A model-independent analysis of electron scattering data for the ^{16}O charge density has been carried out by Sick (1978, private communication). The charge density of ^{16}O calculated by the method described in § 2.2 using two models for the wavefunctions is shown in figure 3. The proton binding energies we have used are given in table 2. In one case (labelled IA in figure 3) we have assumed that ^{16}O is a closed-shell configuration and $R = 3.276$ fm was chosen to reproduce the RMS charge radius. For the other case (labelled RW) we have used the results of shell-model calculations (Reehal and Wildenthal 1973) in which 2p–2h and 4p–4h admixtures are included within a ($1p_{1/2}$, $1d_{5/2}$, $2s_{1/2}$) (psd) model space $R = 3.169$ fm. The proton occupation probabilities in this case are $n(p) = 1.66$, $n(d) = 0.32$, $n(s) = 0.02$ and $n_n = n_p$ (Brown and Wildenthal 1978, unpublished). These psd shell-model calculations differ slightly from the earlier psd calculations of Zuker *et al* (1968, 1969) because of differences in the two-body matrix elements used.

Even though, as shown in figure 3, the calculated result for the closed-shell configuration appears to be closer to experiment, we do not believe that this shows that the closed-shell configuration is more correct. This is because the Woods–Saxon calculation does not include many of the details of the nuclear force such as nonlocality and the many-body aspects that are probably important for the interior density. In fact, one could make a similar comment about Hartree–Fock calculations in which phenomenological interactions such as the Skyrme interaction are used. It has recently been found
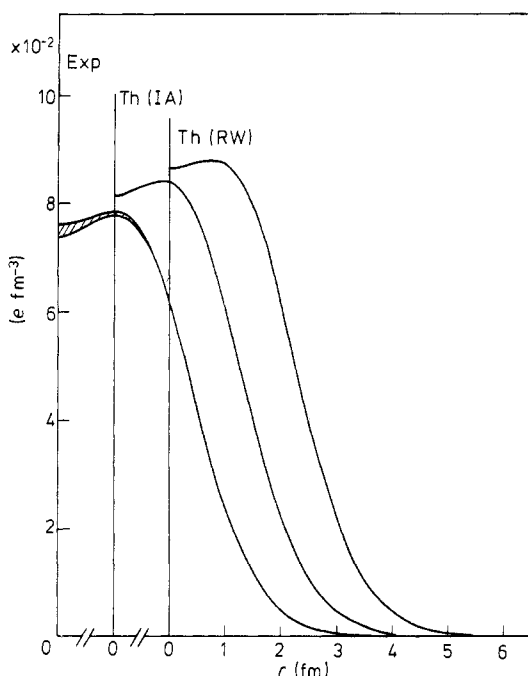

Figure 3. Experimental (Exp) and theoretical (Th) charge densities of ^{16}O. The experimental curves are from Sick (1978, private communication) and represent the upper and lower limits. The densities were calculated with closed-shell (IA) and a non-closed-shell (RW) configuration as discussed in § 3.1.

Table 2. Proton centroid energies for ^{16}O and ^{40}Ca.

Orbit	^{16}O[a]	^{40}Ca[b]
$2p_{3/2}$		-0.13[c]
$1f_{7/2}$		1.21
$1d_{3/2}$		7.59
$2s_{1/2}$	0.10	12.00
$1d_{5/2}$	0.60	19.00
$1p_{1/2}$	12.11	31.50
$1p_{3/2}$	18.44	36.00
$1s_{1/2}$	44.00	48.50

[a] From the binding energy differences between ^{16}O and levels in $A = 15$ and 17, except for the $1s_{1/2}$ state for which the calculated value of Elton and Swift (1967) is used.

[b] From the analysis by Malaguti *et al* (1979) of the spectroscopic factors and energy level centroids from several experiments. For levels near the Fermi surface this analysis takes into account the fragmentation of single-particle strength and hence, for example, the $1d_{3/2}$ binding energy is not exactly equal to the difference in binding energy between the ground states of ^{40}Ca and ^{39}K which is 8.33 MeV.

[c] A value of 0.10 MeV was used for the calculations of the wavefunction.

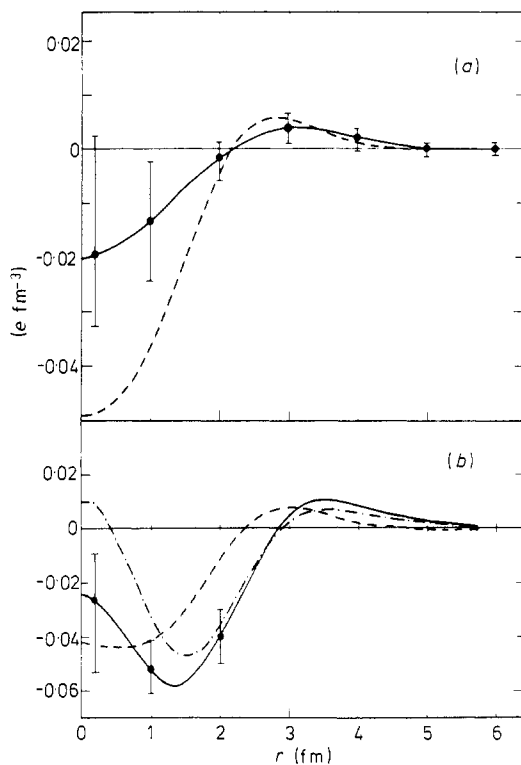**Figure 4.** Experimental (full curves) and theoretical (broken and chain curves) charge density differences $4\pi\Delta\rho(r)_{ch}$ between ^{17}O and ^{16}O (a) and between ^{18}O and ^{16}O (b). The experimental curves are from Miska *et al* (1978). Theoretical curves for ^{17}O and ^{18}O have been calculated with closed 1 s and 1 p shell configurations (IA). In addition, for ^{18}O the calculation was carried out with the schematic wavefunction given by equation (28) which includes proton excitation from the $p_{1/2}$ to the sd orbits (IB). Broken curves, IA; chain curve, IB.
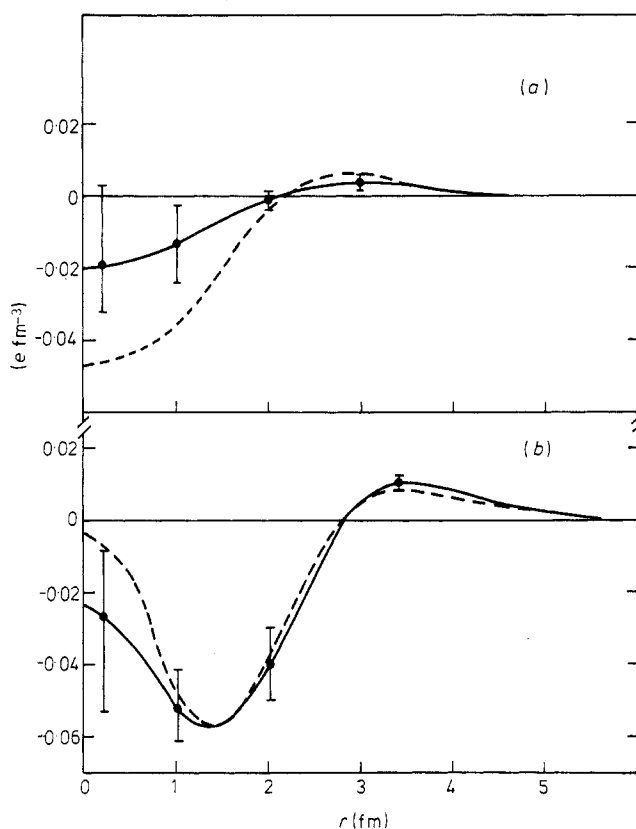
Figure 5. Experimental (full curves) charge density differences $4\pi\Delta\rho(r)_{ch}$ between ^{17}O and ^{16}O (*a*) and between ^{18}O and ^{16}O (*b*) (Miska *et al* 1978) compared with the calculations using occupations probabilities from the Reehal–Wildenthal (RW) wavefunctions (broken curves; see § 3.2). (Note the change in scale between figures 4 and 5 for ^{17}O − ^{16}O.)

that there are many problems associated with calculations of interior densities, as in the cases of ^4He (Arnold *et al* 1978) and of ^{40}Ca discussed below. Perhaps one will need to introduce mesonic degrees of freedom (Negele and Riska 1978, Chertok 1978) in order to understand these problems. Thus, we wish to concentrate in this paper on the density differences which we believe are relatively insensitive to these problems. In this sense the *difference* between the densities IA and RW in figure 3 is important and it represents the correction introduced by the non-closed-shell configurations in ^{16}O.

3.2. The oxygen isotopes

The experimental charge density differences between ^{17}O and ^{16}O and between ^{18}O and ^{16}O have been obtained by Miska *et al* (1979) and their results are shown by the full curves in figures 4 and 5. It turns out, as will be discussed below, that the oxygen charge density differences are well described by the psd shell-model calculations of Reehal and Wildenthal (1973). However, it is instructive to first consider some simpler models for ^{17}O and ^{18}O which have also been widely used. For the calcium isotopes, which will be discussed in § 3.5, the only shell-model calculations which exist are equivalent to these simpler models for ^{17}O and ^{18}O and thus it is important to judge their usefulness.

In the simplest model the ground state of ^{17}O consists of a $1d_{5/2}$ neutron outside an ^{16}O closed shell. The amount of 3p–2h configuration in the difference between ^{16}O and ^{17}O has been determined experimentally to be only 4–6 % (Fortune *et al* 1978). Thus, as a good zeroth-order model for the density difference between ^{17}O and ^{16}O we can take ^{16}O as a closed shell and ^{17}O as a closed shell plus one $1d_{5/2}$ neutron.

The comparison of this model with experiment as shown in figure 4 is not too bad considering that we have taken a very simple configuration and that there are no free parameters in the theory. The change in the experimental RMS radii of $r_{ch}(^{17}O) - r_{ch}(^{16}O) = -0.008 \pm 0.007$ fm from Miska *et al* (1979) and 0.004 ± 0.011 fm from Kim *et al* (1978) is consistent with the calculated value of 0.006 fm. The $^{17}O - ^{16}O$ density difference calculated using the exact psd shell-model occupations will be discussed below.

The difference between ^{18}O and ^{16}O is more interesting. If we consider ^{18}O as simply two neutrons outside ^{16}O then the predicted increase in RMS radius is very small: $r_{ch}(^{18}O) - r_{ch}(^{16}O) = 0.010$ fm (as expected from core polarisation, it is about twice the difference of $^{17}O - ^{16}O$). However, the experimental value is very large: $r_{ch}(^{18}O) - r_{ch}(^{16}O) = 0.074 \pm 0.005$ fm (Miska *et al* 1979).

It is well known, however, that the energy levels and E2 transition rates of ^{18}O cannot be described by two-particle (2p) wavefunctions and that in addition 4p–2h configurations are very important (see Ellis and Engeland 1970, Engeland and Ellis 1972, and references therein). To see the effect of the 4p–2h configurations on the ^{18}O charge density we first consider a simple one-parameter schematic wavefunction similar to that used by Lawson *et al* (1976),

$$|^{18}O\rangle = \alpha|(\nu sd)^2\rangle + \beta|(\pi p_{1/2})^{-2}(\pi sd)^2(\nu sd)^2\rangle, \qquad (28)$$

where $(\nu sd)^2$ represents two neutrons in the sd shell for which we use the occupations calculated with the Chung–Wildenthal interaction (see table 3 below), $(\pi sd)^2(\nu sd)^2$ represents a two-neutron–two-proton $T = 0$ wavefunction for which we use the SU3 approximation (Lawson *et al* 1976) ($n(s) = 0.86$ and $n(d) = 1.14$) and finally $(\pi p_{1/2})^{-2}$ represents two proton holes in the $p_{1/2}$ orbital.

In order to reproduce the experimental change in charge radius we need $\beta^2 = 0.196$, which implies that there are 0.392 fewer protons in the p shell in ^{18}O than there were in ^{16}O. The charge density differences for $^{18}O - ^{16}O$ are shown in figure 4. The simple configuration IA ($\beta^2 = 0$) is in clear disagreement with experiment, especially at the nuclear surface, whereas the more complex configuration IB ($\beta^2 = 0.196$) gives much better agreement.

Lawson *et al* (1976) have determined β^2 in equation (28) from a consideration of many experimental data for ^{18}O, except the electron scattering data, and found $\beta_L^2 = 0.10$. The fact that this is only half the value which we have obtained from the electron scattering data is disturbing. A possible explanation is found if we consider the psd shell-model calculations of Reehal and Wildenthal which include 6p–4h as well as 4p–2h and 2p configurations. In these calculations (Brown and Wildenthal 1978, unpublished) ^{18}O is 64 % of the time in an ^{16}O plus two-particle (2p) configuration, 14 % of the time in an $^{16}O + (4p–2h)$ configuration and 22% of the time in more complex configurations; in these configurations ^{16}O represents the complex psd wavefunction for ^{16}O whose occupations were given in § 3.1. Thus, equation (28) is probably too simple to give a single value of β^2 that explains all the experimental data. In particular, when we consider only electron scattering data β^2 must be chosen so that the simplified wavefunction is forced to give the correct proton orbit occupations and it is very much less sensitive to the neutron orbit occupations.

The only quantity which we can determine is the change in the number of holes in the p shell between ^{18}O and ^{16}O, which we will denote by $\Delta = 2\beta^2 = 0.39$. This can be compared with the values of Δ obtained in shell-model calculations. The Reehal–Wildenthal wavefunctions for ^{16}O and ^{18}O give $\Delta = 0.50$ whereas the psd calculations of Ellis and Engeland, which include only 2p and 4p–2h configurations, give $\Delta = 0.18$. The wavefunction of Lawson *et al* gives $\Delta = 0.20$. In fact, a value of $\Delta \simeq 0.2$ is typical of almost all calculations which include only 2p and 4p–2h configurations, but this is not surprising since shell-model calculations of this type contain single-particle energies and two-body interactions which are chosen rather arbitrarily to give reasonable results for the energy levels and E2 transition rates. Thus our conclusion is that the only wave-functions which have a chance of consistently explaining all data for ^{18}O are those that include 6p–4h components.

Finally, the proton and neutron densities have been calculated using the occupation probabilities determined from the Reehal–Wildenthal wavefunctions. The orbit occupations for ^{16}O are given in § 3.1; for ^{17}O they are $n_p(p) = 1.61$, $n_p(d) = 0.36$, $n_p(s) = 0.03$, $n_n(p) = 1.66$, $n_n(d) = 1.31$ and $n_n(s) = 0.03$, and for ^{18}O $n_p(p) = 1.17$, $n_p(d) = 0.63$, $n_p(s) = 0.20$, $n_n(p) = 1.45$, $n_n(d) = 2.09$ and $n_n(s) = 0.46$. It is interesting to list the valence occupations for ^{17}O: $n^v(^{17}O) = n(^{17}O) - n(^{16}O)$, $n_p^v(p) = -0.05$, $n_p^v(d) = 0.04$, $n_p^v(s) = 0.01$, $n_n^v(p) = 0.00$, $n_n^v(d) = 0.99$ and $n_n^v(s) = 0.01$; this shows that the model of ^{17}O with a $d_{5/2}$ neutron weakly coupled to the ^{16}O core is very good indeed.

The calculated charge density differences are shown in figure 5. The calculated changes in RMS charge radii are $r_{ch}(^{17}O) - r_{ch}(^{16}O) = 0.003$ fm and $r_{ch}(^{18}O) - r_{ch}(^{16}O) = 0.073$ fm compared with the experimental values (Miska *et al* 1979) of -0.008 ± 0.007 fm and 0.074 ± 0.005 fm, respectively. In both cases the agreement is excellent, but to be sure that the small disagreements in the density changes shown in figure 5 are real the present densities should be used to calculate the form factors $F(q^2)$ to compare directly with the experimental data.

3.3. Nuclei with A = 16–30

In this section the general results of our calculations up to $A = 30$ with an ^{16}O core are given. The limit of $A = 30$ was chosen because the programs were designed to include only the $1d_{5/2}$ and $2s_{1/2}$ valence orbits. All stable even–even nuclei were calculated assuming that ^{16}O is a closed shell and that the valence nucleons fill the $1d_{5/2}$, $2s_{1/2}$ and $1d_{3/2}$ (dsd) orbits with occupation probabilities given by the wavefunctions calculated with

Table 3. Valence occupation probabilities for $A = 16$–30 (set IA)[a].

	$n_p(d)$	$n_p(s)$	$n_n(d)$	$n_n(s)$
^{16}O	0	0	0	0
^{17}O	0	0	1	0
^{18}O	0	0	1.659	0.341
^{20}Ne	1.544	0.456	1.544	0.456
^{22}Ne	1.601	0.399	3.567	0.433
^{24}Mg	3.501	0.499	3.501	0.499
^{26}Mg	3.607	0.393	5.396	0.604
^{28}Si	5.273	0.727	5.273	0.727
^{30}Si	5.316	0.684	6.587	1.413

[a] From the shell-model calculations of Chung and Wildenthal (1978 and private communication).

Table 4. Experimental and calculated Barrett radii for $A = 16$–30.

	Experiment				Theory (IA)
	α	k	R_k	$\langle r^k e^{-\alpha r}\rangle$	$\langle r^k e^{-\alpha r}\rangle$
^{16}O	0·048	2·112	3·486(20)[a]	7·132(80)	7·177
^{17}O	0·048	2·112			7·211
^{18}O	0·048	2·114	3·597(25)[b]	7·603(100)	7·248
^{20}Ne	0·051	2·117	3·960(92)	9·124(360)	8·523
^{22}Ne	0·051	2·117			8·312
^{Nat}Ne	0·051	2·117	3·960(92)[a]	9·124(360)	
^{24}Mg	0·054	2·113	3·966(53)	9·018(200)	8·779
^{26}Mg	0·054	2·113			8·574
^{Nat}Mg	0·054	2·113	3·966(53)[a]	9·018(200)	
^{28}Si	0·056	2·112	4·017(4)	9·171(16)	8·872
^{30}Si	0·056	2·112	4·033(6)[b]	9·242(24)	8·701
^{Nat}Si	0·056	2·112	4·0169(38)[c]	9·171(17)	

[a] Engfer et al (1974), table III.
[b] Engfer et al (1974), table IV.
[c] Schaller et al (1978).

the Chung–Wildenthal interaction (Chung and Wildenthal 1978 and private communication). The small occupation of the $d_{3/2}$ orbit was added to that of the $d_{5/2}$ orbit. These occupation probabilities for the d and s orbits are given in table 3.

A compilation of the experimental and calculated Barrett radii is given in table 4. These are then reduced to the equivalent experimental muonic RMS radius $(r_{ch})_\mu$ using equation (27) and compared with the RMS radii from electron scattering in table 5. In this case the accuracy of the electron scattering RMS radii is in general higher. The electron scattering results are plotted in figure 6 and compared with the calculations (open circles).

Table 5. RMS charge radii for $A = 16$–30.

	Experiment		Theory (IA)
	(e, e) r_{ch}	μ atom $(r_{ch})_\mu^{IA}$ [e]	r_{ch}
^{16}O	2·720(4)[a]	2·711(20)	2·720
^{17}O	2·712(5)[a]		2·726
^{18}O	2·794(3)[a]	2·799(20)	2·730
^{20}Ne	3·020(20)[b]	3·090(90)	2·982
^{22}Ne	2·969(21)[b]		2·940
^{24}Mg	3·035(18)[c]	3·091(50)	3·048
^{26}Mg	3·017(32)[d]		3·008
^{28}Si	3·122(11)[c]	3·128(40)	3·075
^{30}Si		3·140(6)	3·043

[a] Miska et al (1979); also Kim et al (1978) give $r_{ch}(^{17}\text{O})/r_{ch}(^{16}\text{O}) = 1·0015 \pm 0·0025$.
[b] deJager et al (1974), table I.
[c] Sick (1978, private communication).
[d] deJager et al (1974), table II.
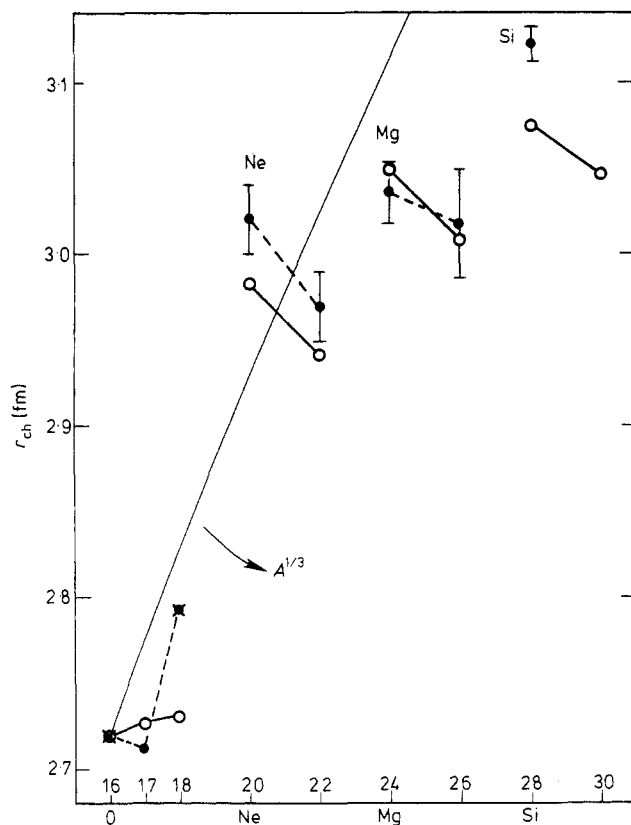[e] Obtained from table 4 using equation (27).

Figure 6. RMS charge radii for $A = 16$–30 nuclei. The experimental data (● – – – ●) are from the electron scattering experiments given in table 5. The theoretical calculations are discussed in §§ 3.1 and 3.2 for ^{16}O, ^{17}O and ^{18}O and in § 3.3 for $A \geqslant 20$. O——O, IA; ×, IB.

The discrepancy concerning ^{18}O was discussed in the previous section. The general trend of the comparison is good, but the large experimental errors preclude a comparison to the same accuracy as was possible for the oxygen isotopes. The systematics of the calculation are easily understood. The large jump between ^{16}O and ^{20}Ne is due to the fact that the two valence protons are put into the fairly loosely bound $1d_{5/2}$ and $2s_{1/2}$ orbits which have large RMS radii compared with that of the core. In ^{20}Ne we find

$$^{20}\text{Ne}: r_\text{p}(1d_{5/2})/r_\text{p}(^{16}\text{O}) = 1\cdot348$$

$$^{20}\text{Ne}: r_\text{p}(2s_{1/2})/r_\text{p}(^{16}\text{O}) = 1\cdot568.$$

As more neutrons are added the proton orbits become more tightly bound until, in ^{28}Si,

$$^{28}\text{Si}: r_\text{p}(1d_{5/2})/r_\text{p}(^{16}\text{O}) = 1\cdot248$$

$$^{28}\text{Si}: r_\text{p}(2s_{1/2})/r_\text{p}(^{16}\text{O}) = 1\cdot321.$$

These results approach the values $1\cdot247$ and $1\cdot247$ obtained in both cases with harmonic oscillator wavefunctions. This accounts for the negative isotopic shift between the pairs of isotopes.
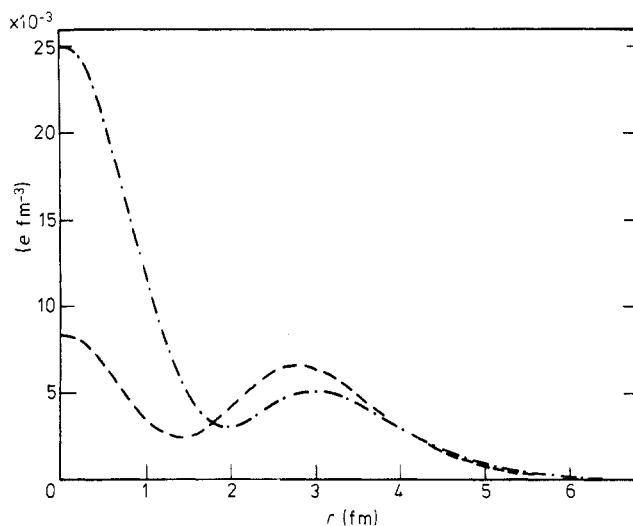
Figure 7. Calculated charge density difference $\Delta\rho(r)_{ch}$ between ^{20}Ne and ^{16}O. A closed-shell configuration has been assumed for ^{16}O and the ^{20}Ne (sd)^4 configuration was obtained from (IA; broken curve) the Chung–Wildenthal wavefunctions (table 3) and from a $(\lambda\mu) = (80)$ SU3 configuration (chain curve) (see § 3.3).
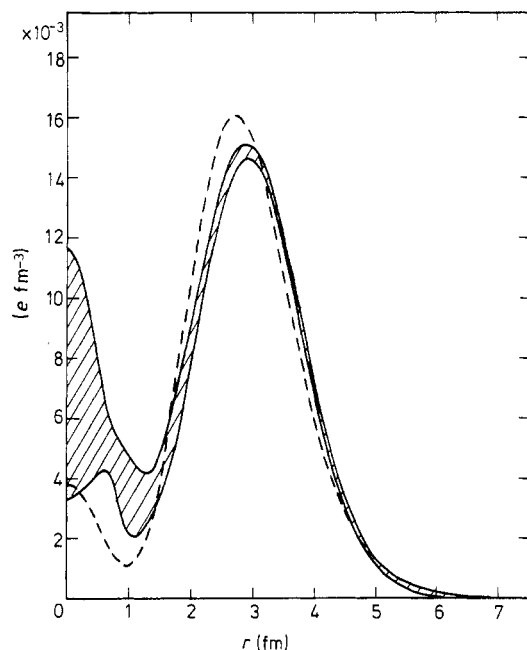

Figure 8. Experimental (full curves) and theoretical (IA, broken curve) charge density difference $\Delta\rho(r)_{ch}$ between ^{24}Mg and ^{16}O. The experimental curves are from Sick (1978, private communication) and are based on the experiments of Li et al (1974). The two curves represent upper and lower limits. For the calculation ^{16}O is assumed to have a closed shell and the ^{24}Mg sd shell occupation probabilities are from table 3 (see § 3.3).

^{20}Ne has also been calculated assuming an SU3 $(\lambda\mu) = (80)$ model for the ^{20}Ne ground state as would be expected in an α–^{16}O cluster model; the occupation probabilities are $n(s) = 0\cdot857$ and $n(d) = 1\cdot143$. The calculated RMS charge radius of $3\cdot012$ fm in this case is in better agreement with experiment, $3\cdot020 \pm 0\cdot020$ fm, than the value of $2\cdot982$ obtained with the Chung–Wildenthal wavefunctions. These two calculations give very different results for the charge density of ^{20}Ne, as is shown in figure 7 which shows the density difference between ^{20}Ne and ^{16}O. Unfortunately there are no experimental data available in this case.

In figure 8 the calculated charge density difference between ^{24}Mg and ^{16}O is shown and compared with experiment. The agreement is very good. One should remember that this curve is the sum of two contributions, one coming directly from the valence proton density which is mostly $d_{5/2}$ in this case and the other from the change in the shape of the 1s and 1p 'core' proton orbits which is due primarily to the interaction with the valence neutrons (the core polarisation effect discussed in § 2.4).

Recently interesting information on the relative RMS radii of the Na isotopes from $A = 21$–31 has been provided by atomic-beam experiments (Huber *et al* 1978). We have not yet made shell-model calculations to obtain the occupation numbers which are needed to calculate the densities for these nuclei. For the Na isotopes with $N = 10$–14 (^{21}Na–^{25}Na) we note that the slope of the decrease in RMS radii matches the slope we predict for the neighbouring Ne and Mg isotopes (see figure 6) which, as mentioned above, is simply due to the increase in the proton binding energies. However, the observed increase in the RMS radii from $N = 14$–20 (^{25}Na–^{31}Na) is probably not reproducible in

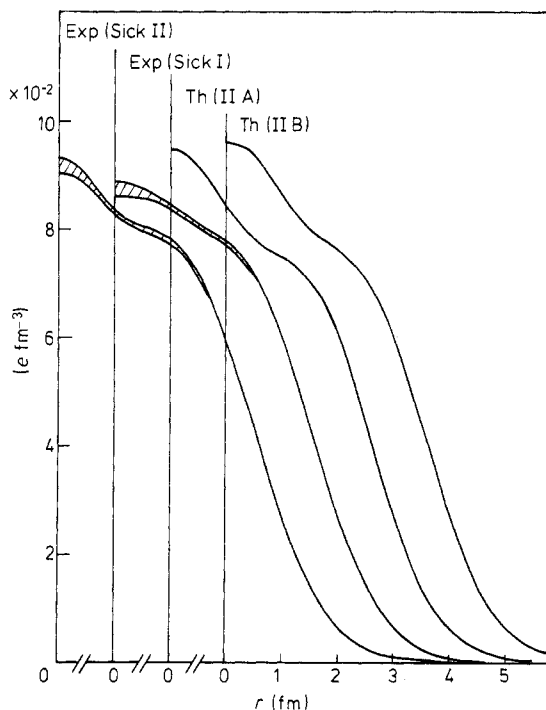**Figure 9.** Experimental and theoretical charge densities $\rho(r)_{ch}$ of ^{40}Ca as discussed in § 3.4. The two sets of experimental curves correspond to the form factor ambiguity discussed by Sick (1974a, 1978, private communication) and each set represents upper and lower limits. IIA and IIB refer to closed-shell and non-closed-shell configurations respectively.

our calculations, as can be seen in figure 6 for our calculations for $N = 14$–16 (^{28}Si–^{30}Si). This change in slope is seen to occur at the $d_{5/2}$ shell closure and the same effect occurs in the fp shell at the $N = 28$ $f_{7/2}$ shell closure (see figure 10 and § 3.6). The probable reason for this failure in our calculations will be discussed at the end of § 3.6.

3.4. The nucleus ^{40}Ca

The experimental charge density of ^{40}Ca is shown in figure 9. The two sets of experimental curves arise from a discrete ambiguity in the analysis of the charge form factor which results from a phase ambiguity in the data around $q \simeq 3.2$ fm (Sick 1974a). Recent experiments at high q transfer have shown that the smoother density (curve I in figure 9) is correct (Frois 1978).

The charge density has been calculated assuming a closed-shell configuration (labelled IIA in figure 9) and a non-closed-shell configuration which will be discussed in detail in § 3.5 (labelled IIB in figure 9); the parameter R is 4·614 fm and 4·562 fm respectively. It is amusing that the calculated shape corresponds closely to the 'incorrect' experimental distribution (II). Hartree–Fock calculations give a shape of the charge distribution nearly identical to the present calculation but with an interior magnitude which is quite sensitive to the interaction (Negele 1970, Campi and Sprung 1972). In all of the calculations the interior bump is due to the filled s orbits.

Thus all calculations for ^{40}Ca show much more interior structure than is found experimentally. As we have indicated in § 3.1 in connection with ^{4}He and ^{16}O, this may mean that the effective many-body interaction is more complicated than the ones which have been inferred from the 'surface' properties of nuclei.

3.5. The calcium isotopes

The Ca isotopes hold a special place in the understanding of nuclear structure. They are the first long chain of stable, experimentally accessible isotopes encountered in the

Table 6. Experimental and calculated Barrett radii for $A = 40$–58.

	Experiment[a]				Theory (IIA)	Theory (IIB)
	α	k	R_k	$\langle r^k e^{-\alpha r} \rangle$	$\langle r^k e^{-\alpha r} \rangle$	$\langle r^k e^{-\alpha r} \rangle$
^{40}Ca	0·065	2·114	4·4609(12)	10·871(6)	10·897	10·851
^{42}Ca	0·065	2·114	4·4998(13)	11·049(6)	10·949	11·052
^{44}Ca	0·065	2·114	4·5126(13)	11·108(6)	10·995	11·091
^{46}Ca	0·065	2·114	4·4881(45)	10·996(21)	11·037	10·972
^{48}Ca	0·065	2·114	4·4621(12)	10·877(6)	11·074	10·865
^{46}Ti	0·068	2·118	4·6261(5)	11·564(3)		11·524
^{48}Ti	0·068	2·118	4·6083(6)	11·482(3)		11·395
^{50}Ti	0·068	2·118	4·5809(5)	11·354(3)		11·281
^{50}Cr	0·071	2·115	4·6947(5)	11·698(3)		11·613
^{52}Cr	0·071	2·115	4·6698(4)	11·586(2)		11·494
^{54}Cr	0·071	2·115	4·7278(5)	11·851(3)		11·456
^{54}Fe	0·074	2·121	4·7387(8)	11·856(4)		11·778
^{56}Fe	0·074	2·121	4·7921(3)	12·112(2)		11·739
^{58}Ni	0·076	2·123	4·8428(6)	12·273(3)		11·952

[a] Ca, Wohlfahrt *et al* (1978); Ti and Cr, Wohlfahrt *et al* (1978, private communication); Fe and Ni, Shera *et al* (1976).

periodic table. ^{40}Ca and ^{48}Ca have shell-model configurations which are closed shells in zeroth order making these two nuclei good candidates for Hartree–Fock calculations. The accurately measured charge RMS radii (Wohlfahrt *et al* 1978) are highly anomalous relative to the smooth *A* dependence found in both the liquid-drop model and the closed-shell Hartree–Fock calculations.

Numerous calculations for the Ca isotopes have been carried out using the standard Woods–Saxon approach (Gibson and Van Oostrum 1967, Elton 1967, Elton and Webb 1970, Malaguti *et al* 1979). Relative to the present calculation the fault of these calculations is that there are too many parameters. Hartree–Fock calculations have been carried out for ^{40}Ca and ^{48}Ca but they do not give very good agreement with experiment (Negele 1970, Bertozzi *et al* 1972). As will be shown below, the probable fault in the conventional Hartree–Fock approach is that non-closed-shell configurations are ignored.

The most accurate experimental data on the RMS radii are provided by the muonic atom experiments. The Barrett radii are given in table 6 and these are converted into equivalent RMS radii using our density shape with equation (27) and the results are given in table 7. The comparison of the RMS radii using a Fermi shape in the muonic atom analysis $((r_{ch})_\mu^F)$ is quite close to the values we infer from the Barrett radii using equation (27) and our density shape $((r_{ch})_\mu^{IIB})$. (Also note that $(r_{ch})_\mu^{IIB} = (r_{ch})_\mu^{IIA}$ to within ± 0.002 fm.)

The RMS radii from table 7 are plotted in figure 10. Additional information is provided by the analysis of electron scattering. The experimental density difference between ^{48}Ca and ^{40}Ca is shown in figure 11. The broken curves are the model-independent analyses of Sick (1974a, 1978, private communication), the two corresponding to the discrete ambiguity of ^{40}Ca of which (I) is correct (Frois 1978). The full curve is the model-dependent analysis of Frosch *et al* (1968) for which a modified Fermi distribution was

Table 7. RMS charge radii for $A = 40$–58.

	Experiment			Theory (IIA)	Theory (IIB)
	(e, e) r_{ch}	μ atom $(r_{ch})_\mu^{Fa}$	μ atom $(r_{ch})_\mu^{IIBb}$	r_{ch}	r_{ch}
^{40}Ca	3·474(3)[c]	3·480	3·479	3·483	3·476
^{42}Ca	3·504[d]	3·510	3·510	3·490	3·510
^{44}Ca	3·502[d]	3·520	3·518	3·497	3·515
^{46}Ca		3·501	3·497	3·503	3·493
^{48}Ca	3·465(5)[c]	3·481	3·475	3·509	3·473
^{46}Ti		3·609	3·608		3·602
^{48}Ti		3·596	3·592		3·578
^{50}Ti		3·574	3·569		3·557
^{50}Cr		3·665	3·661		3·647
^{52}Cr		3·645	3·640		3·625
^{54}Cr		3·690	3·683		3·619
^{54}Fe		3·700	3·695		3·682
^{56}Fe		3·741	3·735		3·675
^{58}Ni		3·781	3·775		3·723

[a] From the analysis in the references given in footnote [a] to table 6 based on a Fermi (F) distribution shape.
[b] Obtained from table 6 using equation (27) and the present density shapes given by IIB.
[c] Sick (1978, private communication).
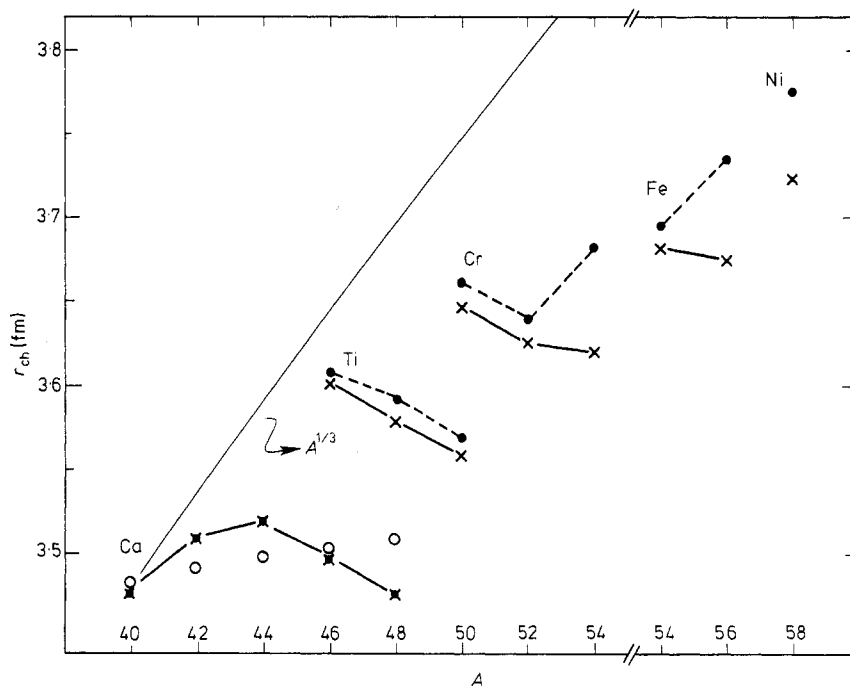[d] Values normalised to ^{40}Ca from Frosch *et al* (1968).

Figure 10. RMS charge radii for $A = 40$–58 nuclei. The experimental ($\bullet$ – – – $\bullet$) and theoretical ($\bigcirc$, IIA; $\times$——$\times$, IIB) results are given in table 7 and discussed in §§ 3.5 and 3.6. Calculation IIA refers to a closed sd shell configuration and calculation IIB allows for excitation out of the sd shell.

assumed. The various densities agree relatively well. The model-dependent densities of Frosch *et al* for ^{42}Ca and ^{44}Ca relative to ^{40}Ca are shown by the full curves in figures 12 and 13 respectively; a model-independent analysis is not available in these cases. It is interesting to note that the magnitudes of the density change relative to ^{40}Ca as shown by the full curves in figures 11, 12 and 13 become progressively larger in going from ^{42}Ca to ^{48}Ca whereas the RMS charge radii of ^{40}Ca and ^{48}Ca are nearly equal.

In our calculation we first consider the situation for a closed sd shell and valence neutrons in the fp shell. We use simplified but realistic (McGrory *et al* 1970) fp shell occupation probabilities of 90 % $1f_{7/2}$ particles plus 10 % $2p_{3/2}$ particles. The results for the RMS radii are given by open circles in figure 10; they have been normalised to ^{40}Ca by choosing $R = 4.614$ fm in equation (17). The isotopic dependence of the RMS radii is small and smooth, in disagreement with experiment. However, the density changes as shown by the chain (labelled IIA) curves in figures 12, 13 and 14 are large and in rough qualitative agreement with experiment.

Hartree–Fock calculations (Negele 1970) have been made with this assumption of a closed sd shell. If we further restrict the neutron configuration in ^{48}Ca to be 100 % $f_{7/2}$ then our calculated proton charge density difference $\Delta\rho(r)_{ch}^{p}$ is similar to the Hartree–Fock results, as shown in figure 15.

Now we consider the amount of excitation of protons from the sd shell to the fp shell which is needed to reproduce the Ca RMS radii. In order to limit the number of parameters we first notice that the density change in the region $r = 0$–1 fm is extremely sensitive to the change in occupation of the $2s_{1/2}$ orbit. The small dip in the centre of the experimental (Sick I) ^{48}Ca $-$ ^{40}Ca density difference shown in figure 11 can be explained
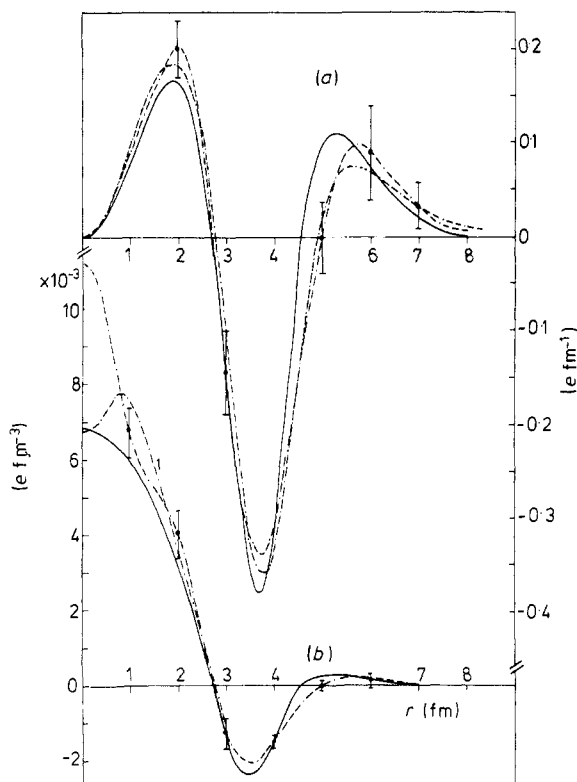
Figure 11. Experimental charge density difference between ^{48}Ca and ^{40}Ca obtained by electron scattering. The full curves are from the model-dependent fit to the data by Frosch *et al* (1968) and the two broken curves are from the model-independent fits of Sick (1974a. 1978. private communication) corresponding to the ambiguity in the ^{40}Ca data shown in figure 9. $--\cdot--\cdot$, Sick I; $-----\cdot----$, Sick II; (a), $4\pi r^2 \Delta\rho(r)_{ch}$; (b), $\Delta\rho(r)_{ch}$.

by a change of only 0·04 particles in the $2s_{1/2}$ orbit between ^{40}Ca and ^{48}Ca. The flat interior density differences for ^{42}Ca and ^{44}Ca obtained by Frosch *et al* shown in figures 12 and 13 indicate that there is no change in the $2s_{1/2}$ occupation probability between ^{40}Ca, ^{42}Ca and ^{44}Ca; however, this is probably due to the restricted Fermi shape used in the experimental analysis and a model-independent analysis of higher-q data would probably reveal interesting interior structure for ^{42}Ca and ^{44}Ca. Nevertheless, for the present data, it will be adequate to assume that the $2s_{1/2}$ orbit is full for all the Ca isotopes.

The Ca isotopes have been studied with the following one-parameter wavefunctions, for $n \geqslant 2$,

$$|^{40+n}Ca\rangle = \alpha |(\nu f_{7/2} p_{3/2})^n\rangle + \beta |(\pi d_{3/2})^{-2}(\pi f_{7/2} p_{3/2})^2 (\nu f_{7/2} p_{3/2})^n\rangle \qquad (29)$$

and for ^{40}Ca

$$|^{40}Ca\rangle = \alpha |0\rangle + \beta |(\pi d_{3/2})^{-1}(\pi f_{7/2} p_{3/2})^1 (\nu d_{3/2})^{-1}(\nu f_{7/2} p_{3/2})^1\rangle \qquad (30)$$

where $|0\rangle$ is the closed-shell configuration. We use this wavefunction schematically to obtain the number of proton holes in the $d_{3/2}$ orbit relative to ^{40}Ca, which is given by

$$\Delta(n) = 2\beta^2(^{40+n}Ca) - \beta^2(^{40}Ca). \qquad (31)$$

As above, it is assumed that the $f_{7/2} p_{3/2}$ configuration is 90% $f_{7/2}$ and 10% $p_{3/2}$.
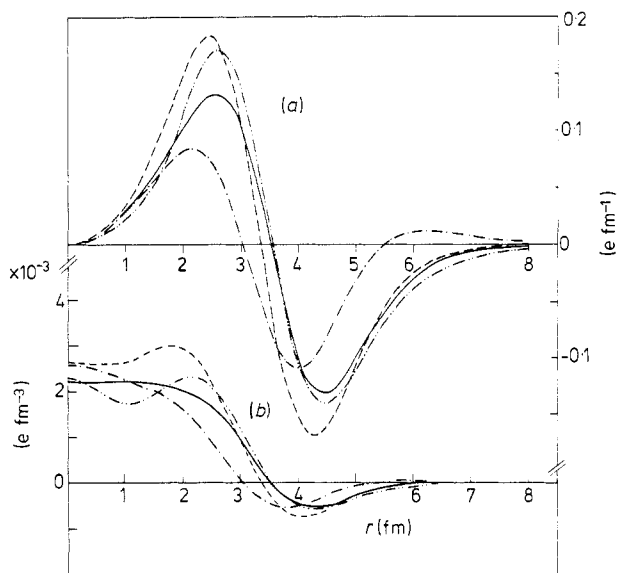
Figure 12. Experimental (full curves) and theoretical (broken curves) charge density differences between ^{42}Ca and ^{40}Ca. The experimental curves are from the model-dependent fit to the electron scattering data by Frosch *et al* (1968). The three theoretical curves correspond to a closed sd shell configuration (— · —, IIA), to a non-closed sd shell configuration with 10% $2p_{3/2}$ (– – –, IIB) and to a non-closed sd shell configuration with 20% $2p_{3/2}$ (– ·· –, IIC) as discussed in § 3.5. (*a*), $4\pi r^2 \Delta\rho(r)_{ch}$; (*b*), $\Delta\rho(r)_{ch}$.
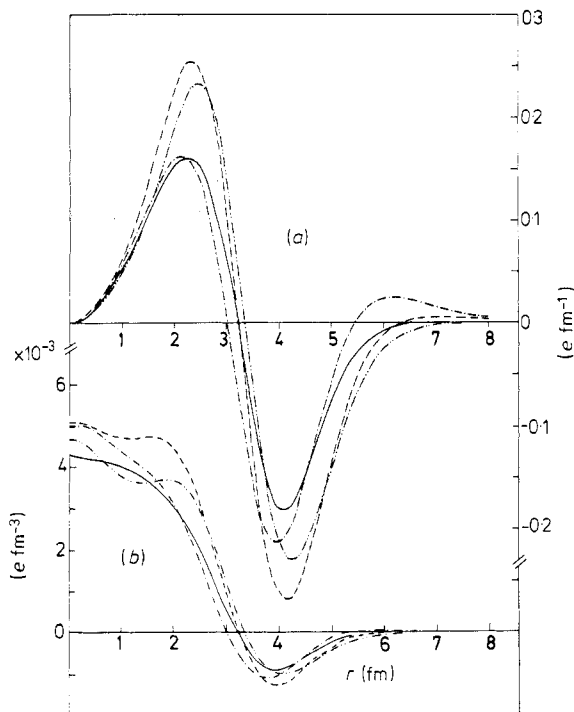

Figure 13. Experimental (full curves) and theoretical (broken curves) charge density differences between ^{44}Ca and ^{40}Ca (see caption to figure 12).
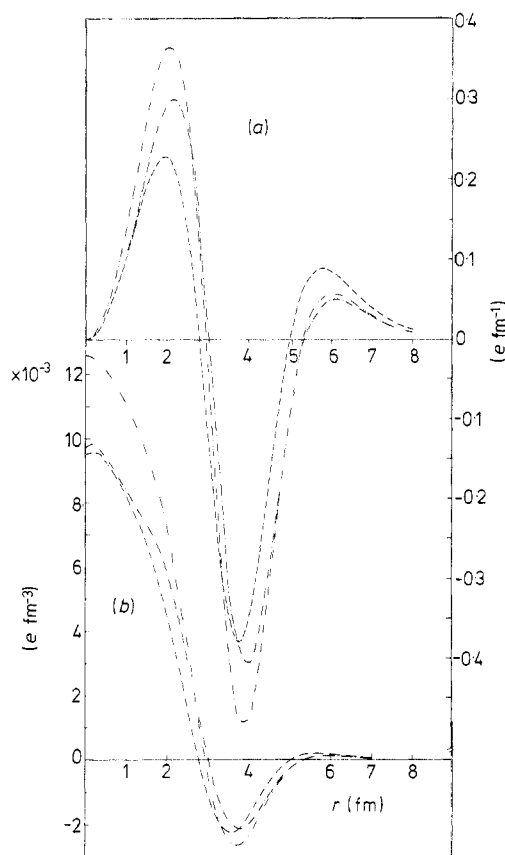
Figure 14. Theoretical charge density differences between ^{48}Ca and ^{40}Ca. $- \cdots -$, $(1f_{7/2})^8$; $- \cdot -$, IIA; $- - -$, IIB. For $- \cdots -$ and $- \cdot -$ a closed sd shell for both ^{48}Ca and ^{40}Ca is assumed and for $- - -$ sd shell core excitations are allowed for as discussed in § 3.5. For $- \cdots -$ the valence neutrons are in a pure $(1f_{7/2})^8$ configuration and for $- \cdot -$ a configuration with 90% $1f_{7/2}$ and 10% $2p_{3/2}$ has been used. (*a*), $4\pi r^2 \Delta\rho(r)_{ch}$; (*b*), $\Delta\rho(r)_{ch}$.

The $\Delta(n)$ are chosen to reproduce the experimental RMS radii for the nuclei from ^{42}Ca to ^{48}Ca and then the density differences are compared with experiment to test our assumptions. For $\Delta(n)$ we find $\Delta(2) = 1\cdot0$, $\Delta(4) = 1\cdot1$, $\Delta(6) = 0\cdot35$ and $\Delta(8) = -0\cdot4$. The negative number for ^{48}Ca $- {}^{40}$Ca is not surprising; it means that there is more core excitation in ^{40}Ca than in ^{48}Ca. The wavefunctions we have used correspond to values of $\beta^2 = 0\cdot7$, $0\cdot85$, $0\cdot9$, $0\cdot525$ and $0\cdot15$ for ^{40}Ca to ^{48}Ca respectively. It should be emphasised that these wavefunctions have little meaning because they do not contain explicitly the more complex four-hole configurations, whereas the values of Δ obviously depend on the total number of proton holes coming from all configurations (see § 3.2).

In figure 14 the calculated difference for the ^{48}Ca $- {}^{40}$Ca charge density is shown for the various approximations which have been used, for a closed sd shell plus eight $f_{7/2}$ neutrons, for a closed sd shell plus an (fp) neutron configuration (IIA) and finally for the $\Delta(8) = -0\cdot4$ configuration (IIB). As pointed out by Bertozzi *et al* (1972), the contributions from the neutron finite size and spin–orbit corrections are important in this case. These corrections have been included in all our calculations as discussed in § 2.5. In figure 16 the spin–orbit correction for the $(1f_{7/2})^8$ configuration is shown and compared with the more realistic (fp)^8 neutron configuration which has 10% $p_{3/2}$. The
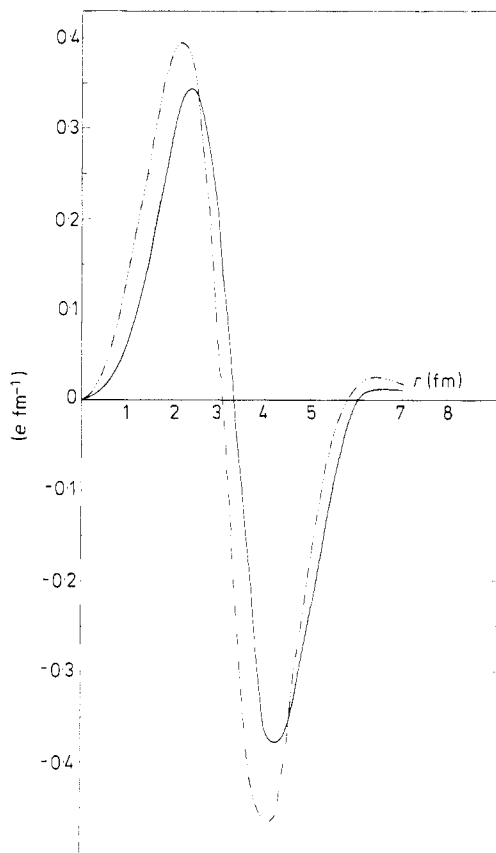
Figure 15. Comparison between the present calculation (–··· –) and the Hartree–Fock calculation of Negele (1970) (—) for the proton charge density difference $4\pi r^2 \Delta\rho(r)^{p}_{ch}$ between ^{48}Ca and ^{40}Ca. The same assumption for the shell-model configuration, namely $(1f_{7/2})^8$ for the valence neutrons, has been made in both calculations.

difference in the central density is significant, but this is a very minor difference between the present and previous calculations compared with the effect of core excitation shown in figure 14.

The calculation with $\Delta(8) = -0.4$ is compared with experiment in figure 17 (Sick I from figure 11). The agreement is excellent; the discrepancy between 0·0 and 1·0 fm could be easily explained if the occupations for the $2s_{1/2}$ orbit were about 1·965 and 2·000 in ^{40}Ca and ^{48}Ca respectively.

A comparison of the calculated and experimental charge density differences for ^{42}Ca $- \ ^{40}$Ca and ^{44}Ca $- \ ^{40}$Ca is shown in figures 12 and 13 respectively. In both cases, but especially for ^{42}Ca, the calculations which include core excitation (IIB) are much improved compared with the closed-shell calculations (IIA), especially in the important surface region. In these figures we give a third calculation (IIC) in which the amount of $2p_{3/2}$ admixture has been increased to 20 % to show the sensitivity to this parameter. A more detailed comparison in these cases must await a better experimental determination of the density change and theoretical calculations of the form factors. For completeness the calculated density change for ^{46}Ca $- \ ^{40}$Ca is shown in figure 18.
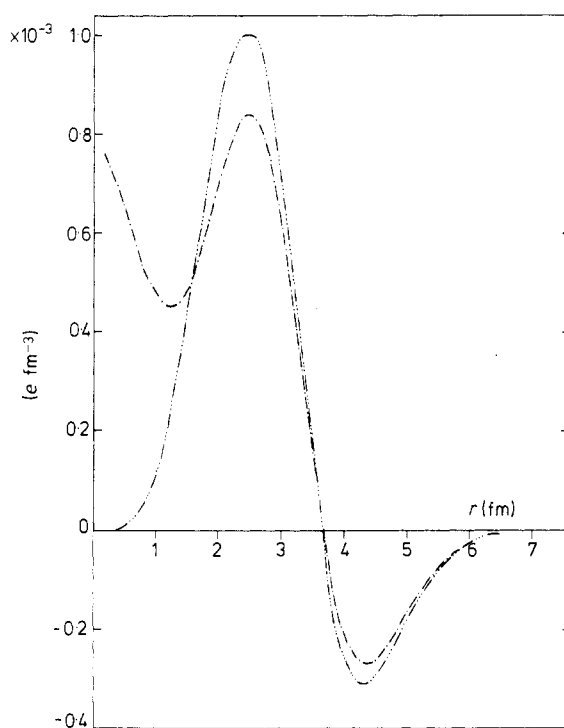
Figure 16. Spin–orbit correction $\Delta\rho(r)^{ls}_{ch}$ to the charge density difference between ^{48}Ca and ^{40}Ca (see §§ 2.5 and 3.5). $- \cdots -$, obtained using a pure $(1f_{7/2})^8$ configuration; $- \cdot -$, obtained using a configuration with 90 % $1f_{7/2}$ and 10 % $2p_{3/2}$ (IA).

Now it is very interesting to compare our values of Δ with other experimental and theoretical determinations of this quantity. One-proton-transfer spectroscopic factors should be a sensitive measure of the number of proton holes and the literature concerning these reactions for the Ca isotopes is extensive. For example, the stripping reaction on ^{42}Ca leading to positive-parity states in ^{43}Sc is a direct measure of the number of proton holes in the sd shell, $H(\text{sd})$, and the pick-up reaction on ^{42}Ca leading to negative-parity states in ^{41}K is a direct measure of the number of proton particles in the fp shell, $P(\text{fp})$. Values of $H(\text{sd})$ and $\overset{\circ}{P}(\text{fp})$ extracted from a sum-rule analysis are given in table 8. If everything has been carried out properly for a given nucleus we should have $\Delta + \delta = P(\text{fp}) = H(\text{sd})$ where δ is chosen to give the absolute number of proton holes in ^{40}Ca and we have rather arbitrarily chosen $\delta = 0.7$. It is seen in table 8 that, in fact, none of these three quantities agree very well. For the stripping and pick-up reactions this is a serious problem which has been pointed out previously (Dehnhard and Cage 1974, Doll *et al* 1976). We feel that the main difficulty is that in order to make use of a sum-rule analysis one must be careful to include all the high-lying levels and to take into account the well known anomalies that result from comparing levels with very different binding energies (Moalem *et al* 1978). The parameter Δ should be the most direct measure of the number of proton holes in the Ca isotopes.

Shell-model calculations for the Ca isotopes which include excitations from the sd shell have been improved progressively, but still seem far from explaining the entire experimental situation. Many calculations have used a $(d_{3/2}, f_{7/2})$ basis. Three different types of calculation have been made for ^{40}Ca within this basis: Gerace and Green (1967,
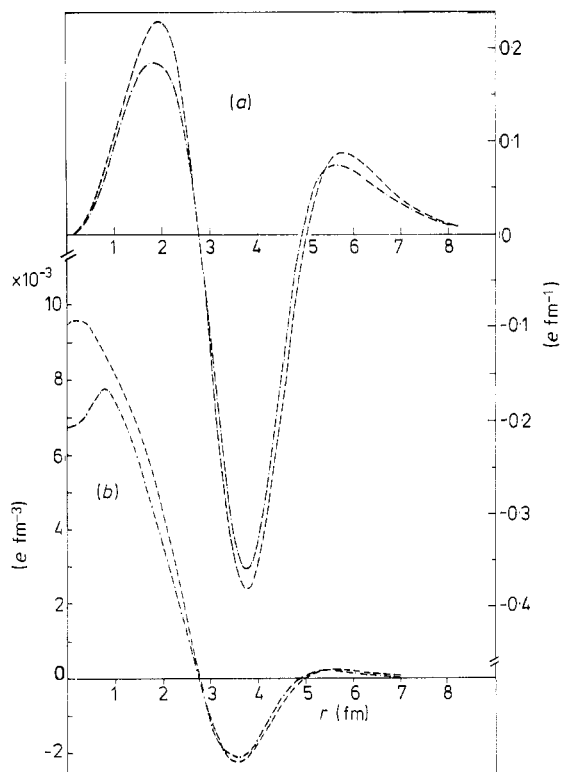
Figure 17. Experimental (— — · — — ·; Sick I) and theoretical (— — —, IIB) charge density difference between ^{48}Ca and ^{40}Ca. The experimental curves are from figure 11 and the theoretical curves are from figure 14. (*a*) $4\pi r^2 \Delta\rho(r)_{\text{ch}}$; (*b*) $\Delta\rho(r)_{\text{ch}}$.
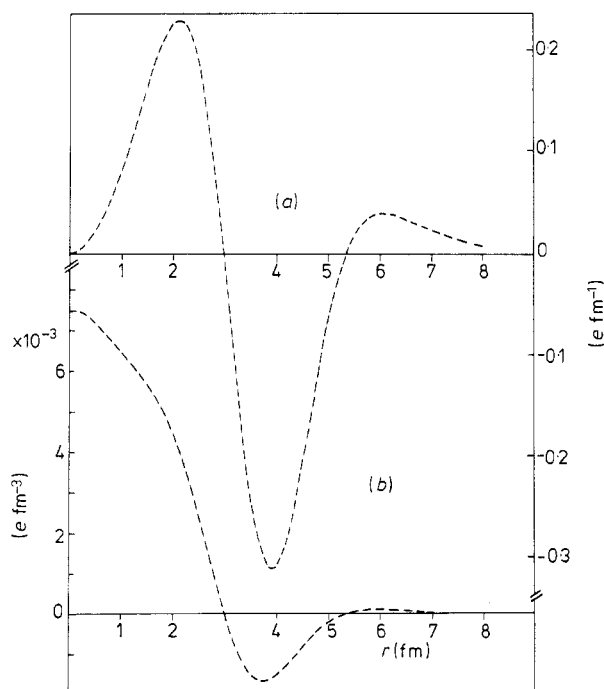
Figure 18. Theoretical (IIB) charge density difference between ^{46}Ca and ^{40}Ca. (*a*) $4\pi r^2 \Delta\rho(r)_{\text{ch}}$; (*b*) $\Delta\rho(r)_{\text{ch}}$.

Table 8. Comparison of the number of proton holes in the sd shell obtained from electron scattering $(\Delta + \delta)$, pick-up reactions $(P(\text{fp}))$ and stripping reactions $(H(\text{sd}))$.

	$\Delta + \delta$	$H(\text{sd})^a$	$H(\text{sd})^b$	$P(\text{fp})^c$	$P(\text{fp})^d$
^{40}Ca	0·7	0·4	0·27	0·73	0·3
^{42}Ca	1·7	0·9	1·12	1·03	0·4
^{44}Ca	1·8	1·9	1·98	1·01	0·6
^{46}Ca	1·05	0·4			0·2
^{48}Ca	0·3	0·15	0·44	0	0

[a] (^{3}He, d), quoted by von der Decken *et al* (1972).
[b] (^{3}He, d), quoted by Doll *et al* (1976).
[c] (d, ^{3}He), Doll *et al* (1976).
[d] (t, α), quoted by Dehnhard and Cage (1974).

1969) have considered configurations up to 8p–8h but in which the $f_{7/2}$ particles are restricted to couple to isospin $T = 0$, Federman and Pittel (1969) and more recently Seth *et al* (1974) have considered configurations up to 4p–4h but allowing all values of T for the $f_{7/2}$ particles, and finally Sakakura *et al* (1976) have used a complete basis (up to 8p–8h with all values of T). The values obtained for the number of proton holes in the $d_{3/2}$ orbit in ^{40}Ca in these three calculations are $\delta = 0·19$, $\delta = 0·53$ and $\delta = 0·76$ respectively. These are consistent with the range of experimental values given in table 8.

It is interesting to compare our value of $\Delta(2) = 1·0$ with the values obtained from these shell-model calculations. Gerace and Green obtain $\Delta(2) = 0·24$ and Seth *et al* obtain $\Delta(2) = 0·37$; both are in poor agreement with the experimental value. The full-basis calculations such as Sakakura *et al* carried out for ^{40}Ca apparently fail completely when they are extended to ^{48}Ca (Gräf *et al* 1978) and the results of these calculations have thus not been reported. It seems, however, that full-basis calculations of this type will be needed in order to understand ^{42}Ca. Flowers and Skouras (1969) considered an extended basis of $(s_{1/2}, d_{3/2}, f_{7/2}, p_{3/2})$ for ^{42}Ca with 2p and 4p–2h components. In two approximations, A and B, they obtain wavefunctions which give $\Delta(2) + \delta = 0·20$ and 0·41 respectively; these are in very poor agreement with the present value of $\Delta(2) + \delta = 1·7$.

In addition to these fully microscopic calculations, simple schematic wavefunctions with two or three components have been constructed in order to understand transition matrix elements and alpha transfer for the Ca isotopes (de Voight *et al* 1974, Towsley *et al* 1973, Fortune and Cobern 1978, Gräf *et al* 1978). The two-component wavefunction which Towsley *et al* use to explain E2 transitions in ^{42}Ca gives $\Delta(2) = 0·52$ and the three-component wavefunction which Fortune and Cobern use to explain alpha transfer to ^{42}Ca gives $\Delta(2) = 0·47$, neither of which is in agreement with the present value of $\Delta(2) = 1·0$ obtained from the ground-state charge radii. However, one must consider whether or not the transition rate and alpha-transfer data could be equally well explained by using wavefunctions with more components with more core excitation. Gräf *et al* have considered two-component wavefunctions to explain the excitation energies and the E0 transition matrix elements to the excited 0^+ states for all of the even–even Ca isotopes. With their wavefunctions they find $\Delta(2) = 1·09$, $\Delta(4) = 0·81$, $\Delta(6) = 0·24$ and $\Delta(8) = -0·08$ (see table 5 of Gräf *et al* 1978), which are in rather good agreement with the present results of 1·0, 1·1, 0·35 and $-0·4$ respectively. However, the value of $\delta = 0·21$ which they obtain for ^{40}Ca seems too small. Thus at present it seems that we need different models to explain different data for the Ca isotopes and clearly the only unified approach to this problem is a careful calculation of all quantities in a large shell-model basis such as has been used by Sakakura *et al* (1976) for ^{40}Ca.

In the conclusion of this section we want again to emphasise the differences between the occupation numbers imposed by the electron scattering data and the occupation

Table 9. Experimental occupation probabilities for ^{40}Ca, ^{42}Ca and ^{44}Ca used for figure 19. The proton occupation probabilities are from Malaguti *et al* (1979) and are based on the one-proton-transfer data summarised by Doll *et al* (1976). Simple neutron configurations are assumed.

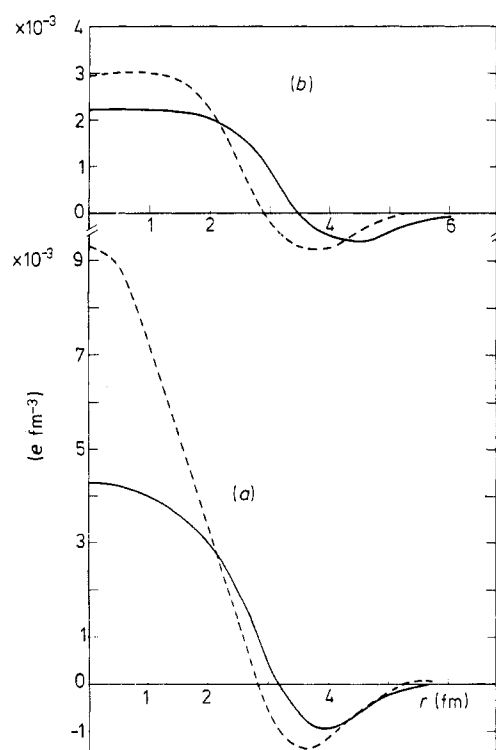|		n_p	n_n
^{40}Ca	$p_{3/2}$	0·15	0·15
	$f_{7/2}$	0·56	0·56
	$d_{3/2}$	3·59	3·59
	$s_{1/2}$	1·70	1·70
^{42}Ca	$p_{3/2}$	0·15	0·20
	$f_{7/2}$	0·92	1·80
	$d_{3/2}$	3·37	4·00
	$s_{1/2}$	1·56	2·00
^{44}Ca	$p_{3/2}$	0·16	0·40
	$f_{7/2}$	0·83	3·60
	$d_{3/2}$	3·57	4·00
	$s_{1/2}$	1·44	2·00

Figure 19. Theoretical charge density differences $\Delta\rho(r)_{ch}$ (broken curves) between (*a*) ^{44}Ca and ^{40}Ca and (*b*) ^{42}Ca and ^{40}Ca as calculated using the experimental occupation probabilities given in table 9 and discussed at the end of § 3.5. The full curves are the experimental results of Frosch *et al* (1968).

numbers obtained from one-proton-transfer experiments. In table 9 we list the 'experimental' occupation probabilities obtained by Malaguti *et al* (1979) from a combination of the stripping and pick-up strengths summarised by Doll *et al* (1976). These occupations have been used to calculate the charge densities, and the differences are plotted in figure 19. First we note that the calculated differences in the RMS charge radii of 0.006 fm and 0.019 fm for ^{42}Ca $- ^{40}$Ca and ^{44}Ca $- ^{40}$Ca, respectively, are not in agreement with the experimental values of 0.031 fm and 0.039 fm, respectively. Secondly the density changes shown in figure 19 are not in good agreement with experiment. In particular, in ^{44}Ca $- ^{40}$Ca the large central peak in the calculated density is due to the large number of holes in the $2s_{1/2}$ orbit in ^{44}Ca. However, it should be remembered that the electron scattering has been analysed with a restricted form for the density. New, less model-dependent, analyses and new experiments of higher q on ^{42}Ca and ^{44}Ca may reveal interesting interior density changes due to the $2s_{1/2}$ orbit.

3.6. Nuclei with A = 40–58

The charge densities of all even–even nuclei in the fp shell up to $A = 58$ have been calculated. Our model certainly breaks down if the number of valence particles is not much less than the number of core particles, but we want to explore this limit with the hope of getting some idea how the model might be improved in this respect, such as by moving towards complete self-consistency.

The experimental and calculated charge moments are listed in tables 6 and 7 and the RMS radii are plotted in figure 10. For the occupation probabilities we have assumed that the amount of proton core excitation is independent of the neutron number. That is, for example, for ^{46}Ti, ^{48}Ti and ^{50}Ti we assume that the number of proton holes in the sd shell relative to ^{40}Ca is the same as it was for ^{44}Ca, ^{46}Ca and ^{48}Ca, respectively, i.e. $\Delta = 1.1, 0.35$ and -0.4 respectively. This simple (but not obvious) requirement on the proton occupations is needed in order to reproduce the experimental trends in the RMS charge radii up to nuclei with 28 neutrons as shown in figure 10. The additional valence protons are put into an fp configuration with 90% $f_{7/2}$ and 10% $p_{3/2}$ occupations.

The indication that the number of proton holes in the sd shell is the same in $^{44}_{20}$Ca$_{24}$ and $^{46}_{22}$Ti$_{24}$ is surprising because one might think that the proton core excitation should be 'blocked' by the additional two protons in the fp shell. However, we note the similarity in the excitation energies of the lowest $\frac{3}{2}^+$ states (proton excitations) in $^{45}_{21}$Sc$_{24}$ at 12 keV and in $^{47}_{23}$V$_{24}$ at 260 keV, those of $^{47}_{21}$Sc$_{26}$ at 766 keV and $^{49}_{23}$V$_{26}$ at 748 keV, and finally those of $^{49}_{21}$Sc$_{28}$ at 2372 keV and $^{51}_{22}$V$_{23}$ at 2677 keV.

The calculated charge density difference for ^{48}Ca $- ^{48}$Ti compared with the experimental analysis of Frosch *et al* (1967) is shown in figure 20. The agreement is very good in this case. One should remember that these curves represent the sum of three distinct effects: (1) an addition of two valence protons to the fp shell which gives the dominant contribution to the density difference, (2) a change in the amount of proton core excitation from the sd shell, and (3) a change in the core polarisation due to the change of two valence protons into two valence neutrons. In figure 20 two theoretical curves are given, one corresponding to 90% $f_{7/2}$ and 10% $p_{3/2}$ (IIB) and the other corresponding to 80% $f_{7/2}$ and 20% $p_{3/2}$ (IIC); a better experimental analysis is needed in order to choose between these two cases.

Finally the nuclei with 30 neutrons have been calculated with a configuration consisting of the configuration of 28 neutrons with the two additional neutrons in the $2p_{3/2}$ orbit. Our calculations for these nuclei are not in good agreement with experiment, as shown in figure 10, and there is no reasonable way to change the occupations to obtain
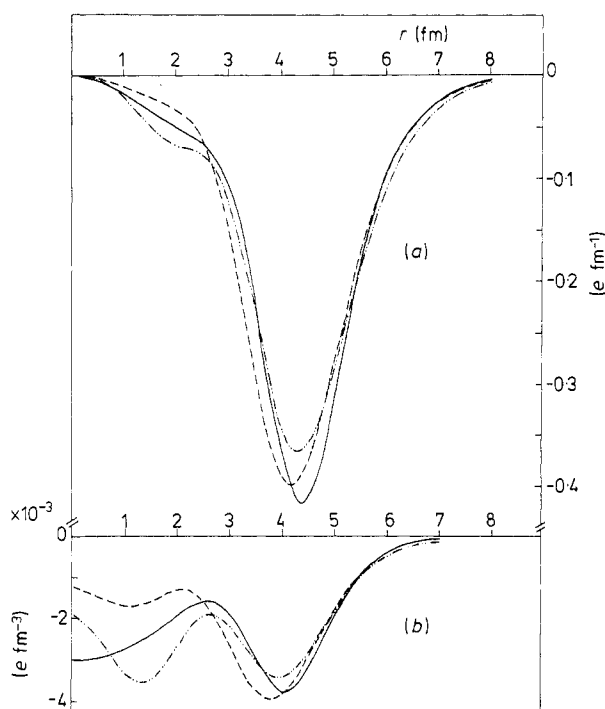
Figure 20. Experimental (full curves) and theoretical (– – –, IIB; $\cdots - \cdots -$, IIC) charge density differences between ^{48}Ti and ^{48}Ca (see § 3.6). The experimental curve is from the model-dependent fit to the electron scattering data by Frosch *et al* (1968). The curves – – – correspond to a 10% $2p_{3/2}$ admixture and the curves $\cdots - \cdots$ correspond to a 20% $2p_{3/2}$ admixture. (*a*) $4\pi r^2 \Delta\rho(r)_{ch}$; (*b*) $\Delta\rho(r)_{ch}$.

agreement. This clearly indicates a limitation on our approach. This is not unexpected since we have only incorporated a self-consistency which is linear in the density, and hence is limited to nuclei close to the 'core' nuclei of ^{16}O and ^{40}Ca. However, it appears that the problem is associated with nuclear saturation. That is, when a change in the density results in a nuclear matter density beyond the saturation of $\rho_0 \sim 0.17$ nucleons/fm^3 a rearrangement occurs that cannot be accounted for by a simple polarisation effect. This may be the situation when the 2p orbit is being filled beyond ^{56}Ni since the 2p orbit has a large interior density at $r \simeq 1.4$ fm. The same situation occurs in the sd shell upon the closing of the $1d_{5/2}$ orbit at $N = 14$. Beyond $N = 14$ the $2s_{1/2}$ orbit is being filled preferentially and a similar rearrangement occurs. This effect has been reproduced by deformed Hartree–Fock calculations in the sd shell (Huber *et al* 1978).

3.7. ^{40}Ca plus or minus one nucleon

We began this section (§ 3.2) with a discussion of the 'single-particle' nucleus ^{17}O and we will end by presenting the results for the four 'single-particle' nuclei surrounding ^{40}Ca. Experiments on the charge density have only been carried out on the stable nucleus ^{39}K (Sick 1974a). Targets of radioactive ^{41}Ca exist, but as yet experiments have not been carried out. The experimental analysis is more complicated for the odd–even isotopes since the electromagnetic interaction can contain magnetic and quadrupole interactions as well as the charge monopole interaction which is the only contribution for $J = 0$ even–even nuclei.

Table 10. Results for $A = 39$ and $A = 41$ relative to ^{40}Ca.

	δ_{ch} (fm)[a]			$r_n - r_p$ (fm)	
	Theory (IID)[b]	Theory (IIE)[c]	Experiment	Theory (IID)[b]	Theory (IIE)[c]
^{40}Ca	0	0		−0·056	−0·056
^{39}Ca	0·100	0·007		−0·088	−0·092
^{41}Ca	0·005	−0·003		−0·018	−0·026
^{41}Sc	0·054	0·041		−0·098	−0·095
^{39}K	−0·018	−0·031	−0·035(11)[d]	−0·032	−0·026
			−0·043[e]		
			−0·039[f]		

[a] $\delta_{ch} = r_{ch}(A) - r_{ch}(^{40}\text{Ca})$.
[b] The extreme single-particle model was assumed for the valence occupation numbers.
[c] The valence occupations for set IIE are given in table 11.
[d] (e, e) (Sick 1978, private communication).
[e] μ atom (Wohlfahrt *et al* 1978, private communication).
[f] The Barrett radii from [c] converted to equivalent RMS radii using equation (27).

The results of calculations for these nuclei are given in table 10. We have used two models for the occupation probabilities. For one we assume that these nuclei can be represented as a single particle or hole 'weakly coupled' to the ^{40}Ca (labelled IID in table 10). For the other we take the valence occupations from the shell-model calculations of Poves *et al* (1977); these are listed in table 11. The results in table 10 depend very little on what is assumed for the ^{40}Ca core itself. For both these calculations we have used the wavefunction given by equation (30) with $\beta^2 = 0·7$.

Usually shell-model calculations are carried out with interactions which do not include a state-dependent two-body Coulomb interaction and for which the nuclear interaction is assumed to be charge symmetric ($V_{pp} = V_{nn}$) and charge independent ($V_{pn} = V_{nn}$ for $T = 1$). In this case the nuclear states have good isospin and the occupation numbers of analogue states can be expressed in the form $n_n = n_0 - T_3 n_1$ and $n_p = n_0 + T_3 n_1$ where n_0 and n_1 are the isoscalar and isovector occupation numbers. However, the shell-model calculations of Poves *et al include* a two-body Coulomb interaction and hence there is no longer a mirror symmetry in the occupation numbers (table 11).

Table 11. Valence occupation probabilities (set IIE) for $A = 39$ and $A = 41$ from the shell-model calculations of Poves *et al* (1977).

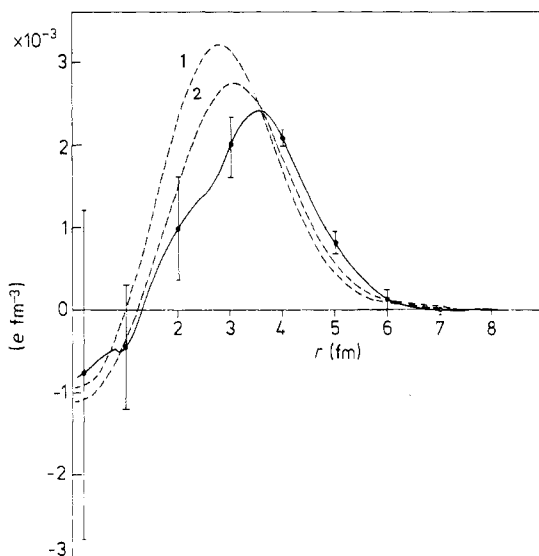|		n_p^v	n_n^v
^{39}Ca	$f_{7/2}$	0·06	−0·26
	$d_{3/2}$	−0·06	−0·74
^{41}Ca	$f_{7/2}$	−0·08	0·71
	$d_{3/2}$	0·08	0·29
^{41}Sc	$f_{7/2}$	0·71	−0·12
	$d_{3/2}$	0·29	0·12
^{39}K	$f_{7/2}$	−0·31	−0·01
	$d_{3/2}$	−0·69	0·01

Figure 21. Experimental (—; Sick II) and theoretical (1, IID; 2, IIE) charge density differences $\Delta\rho(r)_{ch}$ between ^{39}K and ^{40}Ca as discussed in § 3.7. The experimental curve is from the model-independent analysis of the electron scattering data by Sick (1974a, 1978, private communication). The theoretical curve 1 corresponds to a weak-coupling assumption for the $1d_{3/2}$ hole state in ^{39}K and curve 2 corresponds to the ^{39}K occupation probabilities obtained by Poves *et al* (1977) given in table 11.

The charge density difference obtained by Sick for ^{40}Ca $-$ ^{39}K is shown in figure 21. The experimental distribution corresponding to ^{40}Ca (Sick II) in figure 9 has been used, even though as discussed previously ^{40}Ca (Sick I) is correct. This is because the density for ^{39}K has been obtained with a 'type-II' analysis. For ^{39}K it is possible that magnetic scattering is important for the high-q data making it difficult to decide between a 'type-I' fit and a 'type-II' fit. Until a more careful analysis is carried out, it makes more sense to use 'type-II' for both ^{40}Ca and ^{39}K.

The calculated ^{40}Ca $-$ ^{39}K density difference in the weak coupling model (IID) is dominated by the density of the $d_{3/2}$ orbit, but the core polarisation is not negligible. This curve in figure 21 is in poor agreement with experiment. On the other hand, with the shell-model wavefunctions of Poves *et al*, the 'valence' density is distributed 69 % in the $d_{3/2}$ orbit and 31 % in the $f_{7/2}$ orbit and this gives a density difference in better agreement with experiment. The remaining discrepancy between experiment and theory may be due to the $2s_{1/2}$ and $2p_{3/2}$ orbits which were not included in the calculation.

In addition the RMS charge radius change for ^{39}K $-$ ^{40}Ca calculated with (IIE) is in better agreement with experiment than that calculated assuming weak coupling (IID). Thus, weak coupling does not work nearly as well as it does both empirically and theoretically for the 'single-particle' nuclei surrounding ^{16}O as discussed for ^{17}O in § 3.1.

4. Neutron densities

An important feature of the present calculation is the self-consistency between the Coulomb potential and the symmetry potential as discussed in § 2.2. Once the proton

and neutron occupation probabilities and the potential for the protons are fixed, the neutron single-particle energies and densities are determined with the assumption that the nuclear force is charge symmetric, i.e. that the pp and nn nuclear interactions are equal. It is well known that the neutron single-particle energies calculated in this way for mirror nuclei deviate from the experimental values by about 10 % (Nolen and Schiffer 1969). This is also the case in the present calculations and a detailed report of the results for Coulomb energies and the displacement energies of mirror nuclei will be presented elsewhere (Brown *et al* 1979, unpublished). In this section the results for the neutron densities will be discussed and compared with experiment to see if any related anomalies appear.

It is fortunate that for most nuclei considered here the neutron occupations are theoretically well determined relative to the proton occupations. For example, in an $N = Z$ nucleus it is a good assumption that $n_n = n_p$ for each orbit. And in equations (28) and (29) the neutron occupations are independent of β^2 due to the structure of the wave-functions. In contrast there is much less known *a priori* about the neutron occupations in 'closed shell plus or minus one nucleon' nuclei which range from the simple weak-coupling situation in ^{17}O (§ 3.1) to the complex situation for nuclei surrounding ^{40}Ca (§ 3.7).

Hadron scattering cross sections are sensitive to some linear combination of the proton and neutron densities. For proton or alpha scattering the well determined charge density is usually combined in the analysis to determine the difference $r_n - r_p$. This difference has also been determined by comparing π^- and π^+ cross sections. The results for $r_n - r_p$ are summarised in table 12. Also the results for the neutron RMS radii relative to ^{40}Ca are given in table 13. The entries in tables 12 and 13 are representative of the

Table 12. Differences between neutron and proton RMS radii.

	Theory		Experiment					
			1.05 GeV p			1.0 GeV p α	π±	
	Occupation set	$r_n - r_p$ (fm)	a	b	c	d		
^{16}O	RW	−0.041	−0.07(3)					
^{18}O	RW	0.177					0.03(3)[g]	
^{24}Mg	IA	−0.041						
^{26}Mg	IA	0.045						
^{40}Ca	IIB	−0.056	0.02(3)	0.02	−0.04	−0.07		
^{42}Ca	IIB	−0.010	0.08(3)	0.05				
^{48}Ca	IIB	0.168	0.21(3)	0.19	0.19(5)	0.21(5)	0.17(5)[e] 0.08(5)[h]	
							0.17(10)[f]	
^{58}Ni	IIB	−0.020	−0.01(3)	−0.04[i]				

[a] Chaumeaux *et al* (1978), table X.
[b] Alkhazov *et al* (1978), table 6.1.
[c] Varma (1977).
[d] Varma and Zamick (1977).
[e] 1.37 GeV α (Alkhazov *et al* 1977).
[f] 104 MeV α (Friedman *et al* 1978).
[g] Iversen *et al* (1979).
[h] Jakobson *et al* (1977).
[i] For ^{58}Ni Ray *et al* (1978a,b) have obtained $r_n - r_p = -0.036(70)$ fm from 0.8 GeV proton scattering data.

Table 13. Neutron RMS radii relative to ^{40}Ca. $\delta_n \equiv r_n(A) - r_n(^{40}\text{Ca})$.

		Theory		Experiment			
				1·05 GeV p			$\pi^\pm$
ΔN		Occupation set	δ_n (fm)	a	b	c	d
2	^{42}Ca	IIB	0·079	0·09(3)	0·07		
4	^{44}Ca	IIB	0·152	0·13(3)	0·10		0·09(5)
6	^{46}Ca	IIB	0·201				
	^{48}Ti	IIB	0·204		0·18		
8	^{48}Ca	IIB	0·240	0·18(3)	0·16	0·22	0·14(5)
10	^{58}Ni	IIB	0·286	0·25(3)	0·22		

[a] Chaumeaux *et al* (1978), table IX.
[b] Alkhazov *et al* (1978), table 6.1.
[c] Varma (1977).
[d] Jakobson *et al* (1977).

more recent work. A more complete summary of all work has been presented by Chaumeaux *et al* (1978) in table XX of their paper.

It is difficult to assign errors to the radii extracted from hadron scattering experiments; typical values are $\pm 0\cdot05$ fm (Varma 1977, Varma and Zamick 1978) and $\pm 0\cdot07$ fm (Ray *et al* 1978b). If one accepts an uncertainty of at least $\pm 0\cdot05$ fm on all the proton and alpha scattering experimental results for the neutron radii, the agreement between experiment and theory in tables 12 and 13 is fairly good. For the closed-shell nuclei ^{16}O, ^{40}Ca and ^{48}Ca our calculations are also in good agreement with most Hartree–Fock calculations (see table 2.1 of Barrett and Jackson 1977). There is a relatively large disagreement between the present calculation and the proton scattering results of Chaumeaux *et al* (1978) for $r_n - r_p$ in ^{42}Ca; this indicates that neutron excitation from the sd shell is important and a confirmation of this experimental result would be of interest.

It is disturbing that there is such a large scatter in the experimental $r_n - r_p$ values in ^{40}Ca. The values of $r_n - r_p$ in $N = Z$ nuclei are relatively well determined theoretically since the difference is due only to Coulomb effects (the known charge-asymmetric force is much smaller than the Coulomb effect). Since the radial dependence of the Coulomb force in nuclei is dominated by a one-body term proportional to r^2, in an harmonic oscillator basis its effect is simply a scale change in the potential, i.e. $\hbar\omega_p = \alpha\hbar\omega_n$ (Soper 1968). In addition, the dominance of the r^2 term leads to a very simple form for the isovector density difference (Auerbach 1974):

$$\rho_1(r) = C\left(3\rho_0(r) + r\frac{d\rho_0(r)}{dr}\right) \tag{32}$$

where

$$\int \rho_1(r)\,d\tau = 0 \tag{33}$$

and

$$\frac{\int \rho_1(r)r^2\,dr}{\int \rho_0(r)r^2\,dr} = -2C \tag{34}$$

and thus

$$C = -\tfrac{1}{2}(r_n^2 - r_p^2)/(r_n^2 + r_p^2) \simeq -\tfrac{1}{2}(r_n - r_p)/r_p. \tag{35}$$

This simplicity suggests the following procedure for the analysis of hadron scattering on $N = Z$ nuclei. First one can obtain the proton point density from electron scattering experiments (i.e. by correcting for the proton and neutron finite charge distribution). Then for the neutron point density one can use

$$\rho_n(r) = \rho_p(r) + 2C \left| 3\rho_p(r) + r \frac{d\rho_p(r)}{dr} \right| \tag{36}$$

where C is a parameter. In particular, if good fits cannot be obtained from this one-parameter model, this strongly suggests that the analysis (e.g. the impulse approximation) rather than the nuclear density distribution is at fault. In the present calculation for ^{40}Ca we have $C = 0.0077$, but other models may give slightly different values (see § 2.2).

The pion scattering results for $r_n - r_p$ given in table 12 are not in good agreement with the present calculations or with the proton scattering experiments. This may indicate that much more care must be taken in the analysis of these experiments. In particular, since the pion–nucleus interaction is surface-peaked, it may not be a good assumption to relate the surface density to the RMS radius by using a parametrisation of the density. The analysis should be carried out using realistic densities as provided by Hartree–Fock and Woods–Saxon calculations. The sensitivity of $r_n - r_p$ to the pion optical potential has also recently been pointed out (Sternheim and Yoo 1978).

The nucleus ^{48}Ca is particularly interesting because it has one of the largest values for $(r_n - r_p)/r_p = 5.0\%$ of any stable nucleus. Since the neutron–proton nuclear interaction dominates the binding energy one expects in general in a given nucleus that the neutrons and protons arrange themselves so as to have a maximum spatial overlap; hence $\rho_n(r) = (N/Z)\rho_p(r)$ and, in particular, $r_n = r_p$. However, the amount of spatial overlap is limited by the Pauli principle so that without the Coulomb interaction only $N = Z$ nuclei can have $\rho_n(r) = \rho_p(r)$. With the Coulomb interaction the line of stability is shifted to neutron-rich nuclei; hence for the stable nuclei we expect $\rho_n(r) \simeq (N/Z)$ $\times \rho_p(r)$. These general considerations are counteracted by shell structure effects. Thus, for example, we find a very large difference of $(r_n - r_p)/r_p = 6.5\%$ in ^{18}O because the two extra neutrons just begin to fill an open shell. (The proton core excitations in ^{18}O reduce $(r_n - r_p)/r_p$ from 7.4% to 6.5%; in view of the above discussion this is an understandable result.) The nucleus ^{48}Ca is stable because of the extra binding of the doubly-closed-shell configuration but it is relatively far from the line of stability and thus it is not surprising that $r_n - r_p$ is large. The case of ^{48}Ca has recently been discussed by Varma and Zamick (1978), who also carry out simple shell-model calculations and obtain values for $r_n - r_p$ in agreement with those in table 12. In order to explain the anomaly in the displacement energies Friedman and Shlomo (1977) have constructed a charge-symmetric potential which gives $r_n - r_p$ much closer to zero in all nuclei; in particular, for ^{48}Ca they find $r_n - r_p = 0.08$ fm. This is in disagreement with the experimental analysis (table 12) and indicates that the displacement energy anomaly is due to a charge-asymmetric nuclear interaction or to a more subtle nuclear structure effect.

5. RMS radii of valence orbits

There is a final category of experiments with which it is interesting to compare our calculations, namely those which are sensitive to the density of a particular orbit. The cross sections for one-nucleon transfer are very sensitive to the RMS radius of the orbit

of a particular nlj from which the transfer takes place. If one has an independent estimate of the spectroscopic factors involved one can extract relative RMS radii such as those between different nuclei in the $1f_{7/2}$ shell or those between $T_<$ and $T_>$ states of a given nucleus. Sub-Coulomb heavy-ion-transfer experiments are particularly useful since the trajectories can be calculated accurately. In particular, the one-neutron-transfer reactions (^{13}C, ^{12}C) and (^{17}O, ^{16}O) have been used to obtain absolute RMS radii of valence orbits (Jones et al 1974, Durell et al 1976, 1977, Franey et al 1979). Finally, the electron scattering experiments have determined magnetic form factors of odd–even nuclei from which the highest multipole component has been used to extract radii for the odd particle (deWitt Huberts et al 1977, deWitt Huberts 1978).

Results from the experimental analyses are given in table 14. We should remark on some of the uncertainties in these analyses which are not included in the errors. The sub-Coulomb (^{17}O, ^{16}O) and (^{13}C, ^{12}C) reactions must be 'calibrated', that is the amplitudes of the ^{17}O→ ^{16}O + n and ^{13}C→ ^{12}C + n parts of the reaction must be known if one wants to extract information on the target. Due to a change in this calibration (Franey et al 1979) the values for the $1d_{5/2}$ and $2s_{1/2}$ radii quoted by Durell et al (1977) have been increased by about 10% (Durell 1978, private communication) and the new values are quoted in table 14.

For the magnetic electron scattering, corrections for core polarisation and mesonic exchange effects must be taken into account. Since the RMS radii are determined primarily from the shape and not the magnitude of the high-q form factor data, any correction which is equivalent to a q-independent (but perhaps λ-dependent) renormalisation will not be important for the extracted radii. The core polarisation calculations which have been carried out thus far (Arima et al 1978, Arita 1977) give relatively large (up to about 30%) but q-independent quenchings (for a given λ) and hence the effect on the extracted radii is small (less than 1%) (deWitt Huberts 1978). Calculations of the mesonic exchange effects, on the other hand, give a more q-dependent renormalisation (Arima et al 1978, Dubach 1978). In the simple cases of $A = 17$ ($d_{5/2}$) and $A = 41$ ($f_{7/2}$) it was found that for neutrons (protons) the extracted RMS radii were about 2·5% (1·5%) larger when mesonic exchange is included than they were when mesonic exchange is not included (deWitt Huberts 1978). The electron scattering RMS radii given in table 14 do not include the core polarisation and mesonic exchange corrections.

The comparison between experiment and theory is in general good, but there is a systematic tendency for the experimental radii to be 2–6% smaller than those calculated. For the radii obtained from magnetic electron scattering the estimates quoted above for the mesonic exchange correction would bring all experimental results to within about 2% of the theoretical calculations. To be certain that this is not due to a calibration problem in the one-nucleon-transfer experiments it would be interesting to measure the radius of a hole orbit, for example by a ^{40}Ca→ ^{39}Ca reaction. The RMS radius of the $d_{3/2}$ orbit in ^{40}Ca should be closer to the average RMS radius, and hence there is less theoretical uncertainty. The calculated value is $r_n(d_{3/2}) = 3·649$ fm and $r_n(d_{3/2})/r_n = 1·098$ (in the harmonic oscillator limit $r_n(d)/r_n = 1·080$).

The largest anomaly in table 14 is in the comparison of the change in the $1f_{7/2}$ neutron radius between ^{48}Ca and ^{40}Ca from the (d, t) reaction (Friedman et al 1977) which gives $0·17 \pm 0·03$ fm compared with the calculated value of $-0·026$ fm. This will be discussed further and in relationship to Hartree–Fock calculations in the concluding section.

It should be mentioned here that a 2–6% change in the valence radius would have little effect on the calculated Coulomb energy differences between mirror nuclei. The dependence of the direct term in the Coulomb energy on the RMS radii is given

Table 14. RMS radii of valence orbits.

Nucleus	nlj	Theory		Experiment	Experiment/ Theory	Reaction	Reference
		Occupation set	r^b (fm)	r (fm)			
Neutrons							
^{17}O	$1d_{5/2}$	RW	3·512	3·44(4)^c	0·980(11)	^{16}O(^{13}C, ^{12}C)	Franey et al (1979)
	$2s_{1/2}$	RW	4·300	4·07(5)^c	0·947(12)	^{16}O(^{13}C, ^{12}C)	Durell et al (1978)
^{25}Mg	$1d_{5/2}$	IA^a	3·379	3·18(8)	0·941(24)	^{25}Mg(e, e)	Euteneuer et al (1977)
^{41}Ca	$1f_{7/2}$	IIE	4·096	4·00(9)	0·976(22)	^{40}Ca(^{13}C, ^{12}C)	Durell et al (1978)
	$2p_{3/2}$	IIE	4·350	4·24(6)^d	0·975(14)	^{40}Ca(^{13}C, ^{12}C)	Durell et al (1978)
^{49}Ti	$1f_{7/2}$	IIB^a	4·070	4·01(4)	0·985(10)	^{49}Ti(e, e)	deWitt Huberts (1978)
^{44}Ca — ^{40}Ca	$1f_{7/2}$	IIB	0·005	−0·02(8)		Ca(^{17}O, ^{16}O)	Jones et al (1974)
^{48}Ca — ^{40}Ca	$1f_{7/2}$	IIB	−0·026	0·17(3)		Ca(d, t)(t, d)	Friedman et al (1977)
^{48}Ca — ^{40}Ca	$2p_{3/2}$	IIB	−0·069	0·06(7)		Ca(^{17}O, ^{16}O)	Jones et al (1974)
Protons							
^{17}F	$1d_{5/2}$	RW	3·688				
	$2s_{1/2}$	RW	4·986				
^{27}Al	$1d_{5/2}$	IA^a	3·335				
^{41}Sc	$1f_{7/2}$	IIE	4·210				
	$2p_{3/2}$	IIE	4·725				
^{45}Sc	$1f_{7/2}$	IIB^a	4·145				
^{51}V	$1f_{7/2}$	IIB^a	4·093	4·01(4)	0·980(10)	^{51}V(e, e)	deWitt Huberts (1978)^e
^{59}Co	$1f_{7/2}$	IIB^a	4·110	4·00(4)	0·973(10)	^{59}Co(e, e)	deWitt Huberts (1978)^e
^{48}Ca — ^{40}Ca	$1f_{7/2}$	IIB	−0·113	−0·10(5)		Ca(^{3}He, d)	Friedman et al (1977)

^{a} These radii were obtained from the average of values in the neighbouring even–even nuclei. For example, for the $1d_{5/2}$ proton radius in ^{27}Al we used $r = 3·340$ fm and $r = 3·330$ fm from ^{26}Mg and ^{28}Si respectively

^{b} These are the point RMS radii which have been corrected for centre-of-mass motion.

^{c} These values for ^{17}O replace those given by Durell et al (1977) due to a change in the calibration as discussed in § 5. Note also that the values given by Durell et al (1977) have been folded with the nucleon finite size.

^{d} This is for the 1·94 MeV $\frac{3}{2}^-$ level in ^{41}Ca.

^{e} See also deWitt Huberts et al (1977).

approximately by (Brown *et al* 1979, unpublished)

$$\Delta E_C = \frac{6}{5}\frac{e^2 Z}{R}\left[1 - \frac{1}{4}\left(\frac{r_v^2}{r_{ch}^2} - 1\right)\right] \tag{37}$$

where $R = \sqrt{\frac{5}{3}}r_{ch}$ and r_v is the RMS charge radius of the valence orbit. From this equation it is easy to see that in order to explain a 10% anomaly in ΔE_C one needs to change r_v by at least 20% as concluded by Nolen and Schiffer. In addition, the core polarisation contribution tends to reduce the dependence of ΔE_C on r_v (Auerbach 1974) and in the limit of $r_n = r_p$ (Friedman and Shlomo 1977, Shlomo and Friedman 1977) $\Delta E_C \rightarrow 6e^2 Z/5R$, which is the classical liquid-drop limit and does not depend at all on r_v.

6. Summary and conclusions

The model for calculating nuclear densities presented in this paper is in several respects complementary to the Hartree–Fock method. The present model takes full account of the complex configuration mixing found in light nuclei but is only semi-self-consistent because we only allow the potential to vary linearly with the density. In Hartree–Fock the density is fully self-consistent but the configuration is restricted to a single Slater determinant with the particles in the lowest spherical or deformed configuration. For most of the nuclei we have considered the results using the linear density approximation are in good agreement with the Hartree–Fock method when we confine ourselves to the closed-shell configurations assumed in Hartree–Fock. However, the experimental density differences are not well reproduced by these closed-shell calculations and we have found much better agreement by allowing excitations out of the closed shells.

In the region $A = 16$–30 where complete large-basis shell-model calculations are available we have used the occupation probabilities from these wavefunctions to calculate the charge density differences and have found excellent agreement with experiment. In the region $A = 40$–58, where the shell-model calculations are not complete, we have used the occupation probabilities from one-parameter schematic wavefunctions and again have found excellent agreement with the charge densities determined in electron scattering experiments.

The linear density approximation, however, fails to account for the increase in RMS radii beyond nuclei with 14 neutrons in the sd shell and those with 28 neutrons in the fp shell. This is probably a consequence of nuclear saturation when the $2s_{1/2}$ and $2p_{3/2}$ orbits begin to fill in the sd shell and fp shell respectively. It is therefore important to find a modification to the linear density approximation to account for this effect if we want to apply the present method more generally. An alternative would be to generalise the Hartree–Fock procedure to take into account realistic occupation probabilities.

The charge densities are sensitive mainly to the proton occupations and these can also be obtained from one-proton-transfer reactions. For the Ca isotopes the proton occupations determined from the charge densities are consistent with the one-proton-transfer data. However it is not possible to calculate accurate charge densities based on the one-proton-transfer data because of the inconsistency between occupations obtained from stripping and pick-up reactions which exists at present.

In order to provide further comparison with the present calculations, it would be most interesting to improve the electron scattering data on ^{20}Ne, ^{42}Ca, ^{44}Ca and ^{48}Ti. The nucleus ^{20}Ne is the most difficult since it is a gas target, but the charge density of this

nucleus may help us to understand the longstanding dichotomy of sd shell against alpha cluster model for ^{20}Ne. New data or perhaps a better analysis of the old data for ^{42}Ca and ^{44}Ca are needed to see the changes in the interior density which are expected from the depletion of the $2s_{1/2}$ proton occupancy in these nuclei. The density difference between ^{48}Ti and ^{48}Ca shows immediately the fp shell valence density but the present data are not adequate to determine the ratio of the $2p_{3/2}$ to $1f_{7/2}$ occupations.

Even though the charge density differences are understood, the present as well as previous calculations are not able to reproduce the observed oscillations in the total charge density. In some cases such as ^{40}Ca and ^{208}Pb (Frois 1978) the observed density oscillations appear to be damped by about a factor of two compared with the calculations but in contrast the ^{3}He and ^{4}He densities appear to have a central depression, i.e. an enhanced oscillation (Arnold *et al* 1978, McCarthy *et al* 1977). Mesonic exchange corrections may be needed to understand these anomalies; those that have been carried out thus far seem to go in the right direction but are too small (Arnold *et al* 1978, Negele and Riska 1978). If these oscillation anomalies are due to three-body forces it may require an extensive reinvestigation of the phenomenological interactions used in Hartree–Fock calculations in order to understand the interior structure of nuclei; the present interactions have been adjusted to reproduce only the bulk and surface properties of nuclei.

In all cases the neutron densities have been calculated self-consistently relative to the proton densities. For $N = Z$ nuclei the neutron–proton density difference is due to a balance between the Coulomb potential which pushes protons out and the symmetry potential which pulls neutrons and protons together; in all cases $r_p > r_n$. We have suggested a method of analysis for the hadron scattering on $N = Z$ nuclei which makes use of the measured charge density and a one-parameter model for the neutron density relative to the proton density; this method may be useful in 'calibrating' the optical potential.

To illustrate the present status of our knowledge about neutron densities it is interesting to summarise all results for ^{40}Ca and ^{48}Ca including the RMS radii of the $1f_{7/2}$ valence neutrons. In table 15, typical experimental results are compared with the present calculation as well as with Hartree–Fock calculations (Lane *et al* 1978, unpublished). Our results are very similar to the Skryme-IV Hartree–Fock calculation. The Skryme-III

Table 15. Comparison of neutron radii in ^{40}Ca and ^{48}Ca.

	$r_n(1f_{7/2})$			$r_n - r_p$		r_n
	^{40}Ca	^{48}Ca	^{48}Ca $- ^{40}$Ca	^{40}Ca	^{48}Ca	^{48}Ca $- ^{10}$Ca
Experiment	4·00(9)[a]	4·01(4)[b]	0·01(10)	0·02(3)[d]	0·21(3)[d]	0·18(3)[d]
			0·17(3)[c]			
Theory[e] Present	4·096	4·070	−0·026	−0·056	0·168	0·240
HF SIII[f]	3·974	4·069	0·095	−0·044	0·138	0·237
HF SIV	4·149	4·155	0·006	−0·046	0·172	0·254

[a] ^{40}Ca(^{13}C, ^{12}C) (Durell *et al* 1978).

[b] ^{49}Ti (e, e) (deWitt Huberts 1978).

[c] Ca(d, t) and (t, d) (Friedman *et al* 1977).

[d] 1·05 GeV proton scattering (Chaumeaux *et al* 1978).

[e] All calculations have been normalised to the same point proton radius in ^{40}Ca: $r_p = 3·383$ fm.

[f] The Hartree–Fock calculations are from Lane *et al* (1978, unpublished); see also Beiner *et al* (1975).

calculation gives some interesting differences which are in slightly better agreement with experiment for the valence radii but which are in worse agreement for $r_n - r_p$ in ^{48}Ca. The most outstanding discrepancies which must be resolved are for the experimental value of $r_n - r_p = 0.02 \pm 0.03$ fm in ^{40}Ca compared with the calculated value of -0.05 fm and for the experimental value of the change in the $f_{7/2}$ neutron radius determined by the ^{40}Ca(t, d) and ^{48}Ca(d, t) reactions of 0.17 ± 0.03 fm compared with a calculated value of at most 0.10 fm.

The valence radii for neutrons and protons which have been determined from heavy-ion one-nucleon-transfer experiments and magnetic electron scattering are in remarkably good agreement with the present calculations. It has been shown that the Nolen–Schiffer Coulomb shift anomaly can be resolved if $r_n = r_p$ in all nuclei (Shlomo and Friedman 1978). One way to make $r_n = r_p$ is to shrink the valence radius by about 20% (for $A = 41$) but this would be in clear disagreement with the experimental results which are typically only a few per cent smaller than those we have calculated. Another way to make $r_n = r_p$ is to change the core radii; for example, the change in neutron radius between ^{17}O and ^{16}O which we calculate to be $r_n(^{17}\text{O}) - r_n(^{16}\text{O}) = 0.128$ fm must be accompanied by a change of $r_p(^{17}\text{O}) - r_p(^{16}\text{O}) = 0.098$ fm in order to make $r_n = r_p$ in ^{17}O. However, the experimental value for the change in proton radius is only -0.008 ± 0.007 fm (Miska *et al* 1978). Thus from these considerations alone it appears that the Nolen–Schiffer anomaly cannot be accounted for by nuclear structure and that a charge-asymmetric interaction is needed.

References

Alkhazov G D, Bauer T, Bertini R, Bimbot L, Bing O, Boudard A, Bruge G, Catz H, Chaumeaux A, Couvert P, Fontaine J M, Hibou F, Igo G J, Lugol J C and Matoba M 1977 *Nucl. Phys.* A **280** 365
Alkhazov G D, Bauer T, Beurtey R, Boudard A, Bruge G, Chaumeaux A, Couvert P, Cvijanovich G, Duhm H H, Fontaine J M, Garreta D, Kulikov A V, Legrand D, Lugol J C, Saudinos J, Thirion J and Vorobyov A A *Nucl. Phys.* A **274** 443
Alkhazov G D, Belostotsky S L and Vorobyov A A 1978 *Phys. Rep.* **42** 89
Arima A, Horikawa Y, Hyuga H and Suzuki T 1978 *Phys. Rev. Lett.* **40** 1001
Arita K 1977 *Proc. Int. Conf. on Nuclear Structure, Tokyo* Contributed Papers p 252
Arnold R G, Chertok B T, Rock S, Schütz W P, Szalata Z M, Day D, McCarthy J S, Martin F, Mecking B A, Sick I and Tamas G 1978 *Phys. Rev. Lett.* **40** 1429
Auerbach N 1974 *Nucl. Phys.* A **229** 447
Barrett R C 1970 *Phys. Lett.* **33B** 388
Barrett R C and Jackson D F 1977 *Nuclear Sizes and Structure* (Oxford: Clarendon)
Beiner M, Flocard H, Nguyen van Giai and Quentin P 1975 *Nucl. Phys.* A **238** 29
Bertozzi W, Friar J, Heisenberg J and Negele J W 1972 *Phys. Lett.* **41B** 408
Brandt H-W, Heilig K, Knöckel H and Steudel A 1978 *Z. Phys.* A **288** 241
Campi X and Sprung D W 1972 *Nucl. Phys.* A **194** 401
Chandra H and Sauer G 1976 *Phys. Rev.* C **13** 245
Chaumeaux A, Layly V and Schaeffer R 1977 *Phys. Lett.* **72B** 33
—— 1978 *Ann. Phys., NY* **116** 247
Chertok B T 1978 *Phys. Rev. Lett.* **41** 1155
Chung W and Wildenthal B H 1978 to be published
von der Decken A, Dehnhard D, Goldschmidt M, Reiter W, Rieck D, Saathoff W and Wiedner C A 1972 *Phys. Lett.* **41B** 477
Dehnhard D and Cage M E 1974 *Nucl. Phys.* A **230** 393
de Voigt M J A, Cline D and Horoshko R N 1974 *Phys. Rev.* C **10** 1798
deJager C W, de Vries H and de Vries C 1974 *Atomic and Nuclear Data Tables* **14** 479
deWitt Huberts P K A 1978 *Proc. Conf. on Modern Trends in Elastic Electron Scattering, Amsterdam* p 21
deWitt Huberts P K A, Lapikas L, De Vries H, Bellicard J B, Cavedon J M, Frois B, Huet M, Leconte Ph, Nakada A, Phan Xuan Ho, Platchkov S K and Sick I 1977 *Phys. Lett.* **71B** 317

Doll P, Wagner G J, Knöpfle K T and Mairle G 1976 *Nucl. Phys.* A **263** 210

Dover C B and Van Giai N 1972 *Nucl. Phys.* A **190** 373

Dubach J 1978 *Preprint*

Durell J L, Buttle P J A, Goldfarb L J B, Phillips W R, Jones G D, Hooton B W and Ivanovich M 1976 *Nucl. Phys.* A **269** 443

Durell J L, Harter C and Phillips W R 1977 *Phys. Lett.* **70B** 405

Ellis P J and Engeland T 1970 *Nucl. Phys.* A **144** 161

Elton L R B 1967 *Phys. Rev.* **158** 970

Elton L R B and Swift A 1967 *Nucl. Phys.* A **94** 52

Elton L R B and Webb S J 1970 *Phys. Rev. Lett.* **24** 145

Engeland T and Ellis P J 1972 *Nucl. Phys.* A **181** 368

Engfer R, Schneuwly H, Vuilleumier J L, Walter H K and Zehnder A 1974 *Atomic and Nuclear Data Tables* **14** 509

Euteneuer H, Rothhaas H, Schwentker O, Moreira J R, deJager C W, Lapikas L, deVries H, Flanz J, Itoh K, Peterson G A, Webb D V, Barber W C and Kowalski S 1977 *Phys. Rev.* C **16** 1703

Federman P and Pittel S 1969 *Phys. Rev.* **186** 1106

Flowers B H and Skouras L D 1969 *Nucl. Phys.* A **136** 353

Fortune H T, Bishop J N, Medsker L R and Wildenthal B H 1978 *Phys. Rev. Lett.* **41** 527

Fortune H T and Cobern M E 1978 *Phys. Lett.* **77B** 21

Franey M, Lilley J S and Phillips W R 1979 *Nucl. Phys.* A **324** 193

Friar J L and Negele J W 1975 *Advances in Nuclear Physics* **8** 219

Friedman E, Gils H J, Rebel H and Majka Z 1978 *Phys. Rev. Lett.* **41** 1220

Friedman E, Moalem A, Suraqui D and Mordechai S 1977 *Phys. Rev.* C **15** 456

Friedman E and Shlomo S 1977 *Z. Phys.* A **283** 67

Frois B 1978 *Proc. Conf. on Modern Trends in Elastic Electron Scattering, Amsterdam* p 1

Frosch R F, Hofstadter R, McCarthy J S, Nöldeke G K, van Oostrum K J, Yearian M R, Clark B C, Herman R and Ravenhall D G 1968 *Phys. Rev.* **174** 1380

Gerace W J and Green A M 1967 *Nucl. Phys.* A **93** 110

—— 1969 *Nucl. Phys.* A **123** 241

Gibson B F and Van Oostrum K J 1967 *Nucl. Phys.* A **90** 159

Gräf H D, Feldmeier H, Manakos P, Richter A, Spamer E and Strottman D 1978 *Nucl. Phys.* A **295** 319

Huber G, Touchard F, Buttgenbach S, Thibault C, Klapisch R, Duong H T, Liberman S, Pinard J, Vialle J L, Juncar P and Jacquinot P 1978 *Phys. Rev.* C **18** 2342

Iverson S, Nann H, Obst A, Seth K K, Tanaka N, Morris C L, Theissen H A, Boyer K, Cottingame W, Moore C F, Boudrie R and Dehnhard D 1979 *Phys. Lett.* **82B** 51

Jakobson M J *et al* 1977 *Phys. Rev. Lett.* **38** 1201

Jones G D, Durell J L, Lilley J S and Phillips W R 1974 *Nucl. Phys.* A **230** 173

Kim J C, Hicks R S, Yen R, Auer I P, Caplan H S and Bergstrom J C 1978 *Nucl. Phys.* A **297** 301

Lawson R D, Serduke F J D and Fortune H T 1976 *Phys. Rev.* C **14** 1245

Lee H C and Cusson R Y 1972 *Ann. Phys., NY* **72** 353

Li G C, Yearian M R and Sick I 1974 *Phys. Rev.* C **9** 1861

Malaguti F, Uguzzoni A, Verondini E and Hodgson P E 1978 *Nucl. Phys.* A **297** 287

—— 1979 *Nuovo Cim.* A **49** 412

McCarthy J S, Sick I and Whitney R R 1977 *Phys. Rev.* C **15** 1396

McGrory J B, Wildenthal B H and Halbert E C 1970 *Phys. Rev.* C **2** 186

Meyers W D 1978 *The Droplet Model (New York: Plenum)*

Millener D J and Hodgson P E 1973 *Nucl. Phys.* A **209** 59

Miska H, Norum B, Hynes M V, Bertozzi W, Kowalski S, Rad F N, Sargent C P, Sasanuma T and Berman B L 1979 *Phys. Lett.* **83B** 165

Moalem A, van Hienen J F A and Kashy E 1978 *Nucl. Phys.* A **307** 277

Negele J W 1970 *Phys. Rev.* C **1** 1260

Negele J W and Riska D O 1978 *Phys. Rev. Lett.* **40** 1005

Nolen J A and Schiffer J P 1969 *Ann. Rev. Nucl. Sci.* **19** 471

Perey F G 1963 *Direct Interactions and Nuclear Reaction Mechanisms* (New York: Gordon and Breach) p 125

Poves A, Cedillo A L and Gomez J M G 1977 *Nucl. Phys.* A **293** 397

Ray L, Hoffman G W, Blanpied G S, Coker W R and Liljestrand R P 1978a *Phys. Rev.* C **18** 1756

Ray L, Rory Coker W and Hoffman G W 1978b *Phys. Rev.* C **18** 2641

Sakakura M, Arima A and Sebe T 1976 *Phys. Lett.* **61B** 335

Schaller L A, Dubler T, Kaeser K, Rinker G A, Robert-Tissot B, Schellenberg L and Schneuwly H 1978 *Nucl. Phys.* A **300** 225

Seth K K, Saha A, Benenson W, Lanford W A, Nann H and Wildenthal B H 1974 *Phys. Rev. Lett.* **33** 233

Shera E B, Ritter E T, Perkins R B, Rinker G A, Wagner L K, Wohlfahrt H D, Fricke G and Steffen R M ~ 1976 *Phys. Rev.* C **14** 731

Sick I 1974a *Phys. Lett.* **53B** 15

—— 1974b *Nucl. Phys.* A **218** 509

Sick I, Bellicard J B, Bernheim M, Frois B, Huet M, Leconte Ph, Mougey J, Phan Xuan-Ho, Royer D and Turck S 1975 *Phys. Rev. Lett.* **35** 910

Shlomo S and Friedman E 1977 *Phys. Rev. Lett.* **39** 1180

Soper J M 1968 *Isospin in Nuclear Physics* ed D H Wilkinson (Amsterdam: North-Holland) p 229

Sprung D W L, Martorell L J and Campi X 1976 *Nucl. Phys.* A **268** 301

Sternheim M M and Yoo K-B 1978 *Phys. Rev. Lett.* **41** 1781

Towsley C W, Cline D and Horoshko R N 1973 *Nucl. Phys.* A **204** 574

Varma G K 1977 *Bull. Am. Phys. Soc.* **22** 1009

Varma G K and Zamick L 1977 *Phys. Rev.* C **16** 308

—— 1978 *Nucl. Phys.* A **306** 343

Wohlfahrt H D, Shera E B, Hoehn M V, Yamazaki Y, Fricke G and Steffen R M 1978 *Phys. Lett.* **73B** 131

Zuker A P 1969 *Phys. Rev. Lett.* **23** 983

Zuker A P, Buck B and McGrory J B 1968 *Phys. Rev. Lett.* **21** 39